J. Fluid Mech. (2021), *vol*. 908, A38. © The Author(s), 2020.
Published by Cambridge University Press
doi:10.1017/jfm.2020.801

Pinch-off of a surfactant-covered jet

Hansol Wee[1], Brayden W. Wagoner[1], Vishrut Garg[1],‡, Pritish M. Kamat[1],§ and Osman A. Basaran[1],†

[1]Davidson School of Chemical Engineering, Purdue University, West Lafayette, IN 47907, USA

(Received 15 July 2020; revised 13 September 2020; accepted 14 September 2020)

Surfactants at fluid interfaces not only lower and cause gradients in surface tension but can induce additional surface rheological effects in response to dilatational and shear deformations. Surface tension and surface viscosities are both functions of surfactant concentration. Measurement of surface tension and determination of its effects on interfacial flows are now well established. Measurement of surface viscosities, however, is notoriously difficult. Consequently, quantitative characterization of their effects in interfacial flows has proven challenging. One reason behind this difficulty is that, with most existing methods of measurement, it is often impossible to isolate the effects of surface viscous stresses from those due to Marangoni stresses. Here, a combined asymptotic and numerical analysis is presented of the pinch-off of a surfactant-covered Newtonian liquid jet. Similarity solutions obtained from slender-jet theory and numerical solutions are presented for jets with and without surface rheological effects. Near pinch-off, it is demonstrated that Marangoni stresses become negligible compared to other forces. The rate of jet thinning is shown to be significantly lowered by surface viscous effects. From analysis of the dynamics near the pinch-off singularity, a simple analytical formula is derived for inferring surface viscosities. Three-dimensional, axisymmetric simulations confirm the validity of the asymptotic analyses but also demonstrate that a thinning jet traverses a number of intermediate regimes before eventually entering the final asymptotic regime.

Key words: capillary flows

1. Introduction

Surfactants are routinely used in diverse applications involving interfacial or free-surface flows. Well-known examples of such applications include: (*a*) coating flows (Schunk & Scriven 1997; Shen *et al.* 2002), (*b*) flow through porous media as in enhanced oil recovery where they are used to help mobilize or displace oil that is trapped in the pores of crude-oil-containing rock formations (Ahmadi, Galedarzadeh & Shadizadeh 2015; Negin, Ali & Xie 2017), (*c*) treatment of respiratory distress syndrome where surfactants are injected into the lungs to enable inflation of alveoli and prevent them from collapsing (Notter 2000; Zasadzinski *et al.* 2001), (*d*) crop spraying where surfactants facilitate spreading of agricultural chemicals on the leaves of plants (Zhang & Basaran 1997) but

† Email address for correspondence: obasaran@purdue.edu
‡ Present address: Air Products, Allentown, PA 18195, USA.
§ Present address: Dow, Inc., Lake Jackson, TX 77566, USA.

also affect in a complex way the sizes and distributions of sizes of spray drops (Kooij *et al.* 2018) which may lead to increased spray drift or pollution (Hilz & Vermeer 2013) and (*e*) during drop formation in myriad applications including ink jet printing (Basaran 2002; Basaran, Gao & Bhat 2013; Castrejon-Pita *et al.* 2013). The primary action of surfactants in these flows is attributable to their preferential adsorption onto interfaces and the concomitant lowering of surface tension, and hence capillary pressure, by their presence at interfaces. However, surfactant concentration is often non-uniform at an interface in a free-surface flow because of interfacial area change by compression or expansion due to normal dilatation and tangential stretching, and surfactant transport by convection and diffusion. Gradients in surfactant concentration give rise to gradients in surface tension and hence tangential interfacial – Marangoni – stresses. In addition to the lowering of surface tension – the soluto-capillary effect – and the Marangoni effect, surfactants may also induce surface rheological effects (Berg 2010) as surfactant molecules are transported along an interface and give rise to frictional losses as the molecules deform against one another. While the implication of these effects has been investigated in some interfacial flows such as coating flows (Scheid *et al.* 2010, 2012), only a handful studies to date have considered the effects of surface rheology on interface pinch-off or breakup (see below). The major goal of this paper is to advance the understanding of the effects of surface viscosities in jet breakup.

While the understanding of the role of the soluto-capillary and Marangoni effects on the breakup of jets of Newtonian fluids is fairly complete (Ambravaneswaran & Basaran 1999; Craster, Matar & Papageorgiou 2002; Timmermans & Lister 2002; Liao, Franses & Basaran 2006; Xu, Liao & Basaran 2007; Roché *et al.* 2009; de Saint Vincent *et al.* 2012; Kovalchuk, Nowak & Simmons 2016; Kamat *et al.* 2018; Martínez-Calvo *et al.* 2020), the understanding of the role of surface viscosities on pinch-off by comparison is in its infancy. The reason for the disparity in the understanding of jet breakup with and without surface rheological effects is due in part to the difficulty in measuring the rheological properties of interfaces in comparison to surface tension. In the absence of surfactants or for clean interfaces, surface tension is a material property that simply depends on the thermodynamic state (Berg 2010). In the presence of surfactants, surface tension is lower than that when the interface is clean and is reduced by an amount that depends on the local surfactant concentration. As summarized in a number of review articles and books (Franses, Basaran & Chang 1996; Tricot 1997; Berg 2010), there now exist numerous robust methods for accurately measuring the surface tension of clean as well as surfactant-laden interfaces.

In the presence of surface rheological effects, the standard framework is to describe the interface as a compressible two-dimensional Newtonian fluid with surface shear and dilatational viscosities obeying the Boussinesq–Scriven equations (Scriven 1960). However, in contrast to measuring surface tension, measurement of material properties of interfaces has proven elusive. For example, Stevenson (2005) has catalogued in a review article that, in measurement of surface shear viscosity, researchers have reported values that differ by orders of magnitude. The surface viscosities are typically measured by monitoring the mechanical response of micro-scale probes to interfacial flows. One possible reason for the discrepancies in measurements may be that many methods generate a mixed interfacial flow, with both shear and dilatational components, and the surface shear and dilatational viscosities cannot be unambiguously determined from measurements of a single mixed-type flow (Elfring, Leal & Squires 2016). Another complication comes from the fact that the flows induced in different experiments often give rise to surface tension gradients and it is then virtually impossible to separate the contributions of the resulting Marangoni stresses from those due to surface viscosities.

Zell *et al.* (2014) have shown that a rotational shear flow can be created without inducing Marangoni stresses. However, the situation appears much more complicated and ambiguous in dilatational flows in that they are almost always accompanied by Marangoni stresses (Elfring *et al.* 2016).

Motivated by the need to improve the understanding of the breakup of surfactant-covered jets as well as drops in the presence of surface rheological effects and at the same time develop a simple yet robust method for measuring surface viscosities, we analyse theoretically in this paper the pinch-off dynamics of a jet of an incompressible Newtonian liquid that is surrounded by a passive gas, e.g. air, in the situation in which the liquid–gas interface is covered with a monolayer of insoluble surfactant. One attractive feature of this flow with respect to measurement of surface viscosities is that Marangoni stress can be shown to be subdominant to other stresses and hence is negligible as the jet approaches pinch-off. Despite the wide-ranging practical and fundamental importance of jet and drop breakup (Eggers 1997; Basaran 2002; Eggers & Villermaux 2008; Basaran *et al.* 2013; Castrejon-Pita *et al.* 2013), surprisingly little work has been done on the problem of pinch-off when surface rheological effects play a role. For example, Ponce-Torres *et al.* (2017) have recently shown that the increase in surfactant accumulation in satellite droplets during drop formation cannot be explained without accounting for surface viscosities. Martínez-Calvo & Sevilla (2018) have shown that surface viscosities have a stabilizing influence on the dynamics in the Rayleigh–Plateau instability of liquid jets covered with a monolayer of insoluble surfactant. Wee *et al.* (2020) have analysed the breakup of a surfactant-covered jet undergoing Stokes flow. Since it is now well known that jet breakup when the interface is either clean (Eggers 1993; Lister & Stone 1998; Basaran 2002; Eggers 2005; Castrejón-Pita *et al.* 2015; Li & Sprittles 2016) or covered with surfactants but where surface rheological effects are absent (Liao *et al.* 2006; Kamat *et al.* 2018) must asymptotically always involve inertia, a major goal of this paper is to extend the results of Wee *et al.* (2020) to situations in which inertia is present.

The paper is organized as follows. Section 2 describes the mathematical formulation of the problem. First, the three-dimensional but axisymmetric (3DA) or two-dimensional (2-D) system of equations, boundary conditions, and initial conditions governing the thinning and pinch-off of a Newtonian jet whose surface is covered with a monolayer of insoluble surfactant is presented. Next, since the jet profile in the vicinity of the pinch-off singularity is expected to be slender, a spatially one-dimensional (1-D) set of slender-jet evolution equations are derived that governs the dynamics of capillary thinning and breakup. In the following section, scaling laws are obtained for jets first in the absence (§ 4.1) and then in the presence (§ 4.2) of surface rheological effects. Self-similar solutions are obtained for the interface shape, surfactant concentration, and fluid velocity where these variables have a scaling form with a power-law dependence on time remaining until pinch-off with universal scaling exponents. The results presented in this section constitute the extension of Eggers' (1993) seminal analysis on the 'universal pinching of 3-D axisymmetric free-surface flow' to situations where surfactants are present and when surface rheology is either absent or present. In the laboratory, the final Eggers-like inertial–viscous (IV) regime in the presence of surfactants may only be reached after a real jet goes through a number of intermediate scaling regimes. Thus, in § 5, results of 3DA simulations are reported where a real jet transitions between a number of intermediate regimes but ultimately asymptotically tends to the counterpart of Eggers' IV regime albeit with surface rheological effects accounted for as discussed in § 4.2. The main body of the paper ends in § 6 with concluding remarks and a brief discussion on possible directions for future studies. In a couple of appendices, we also elucidate the consequences of adopting a nonlinear as opposed to a linear constitutive equation for relating surface viscosity

to surfactant concentration and analyse the effect of initial conditions on surfactant concentration in capillary thinning of jets. It should be noted that consideration of these latter two topics as well as accounting for inertia and solving the 2-D as well as the 1-D system of equations governing capillary thinning as opposed to only the 1-D slender-jet equations differentiate the present paper from the recent publication by Wee *et al.* (2020).

2. Problem formulation

2.1. *Mathematical statement and 3DA equations*

The system is isothermal and consists of an infinite liquid column or jet of an incompressible Newtonian fluid of constant density ρ and constant viscosity μ of unperturbed radius R that is surrounded by a dynamically passive ambient gas that simply exerts a constant pressure on the jet which is taken here to be the pressure datum. The surface of the jet – the liquid–gas (L–G) interface – is covered with a monolayer of an insoluble surfactant and the surface tension of the L–G interface when it is devoid of surfactant is given by σ_p (figure 1). The dynamics is taken to be axisymmetric about the centreline of the initially cylindrical column. Thus, it proves convenient to use a cylindrical coordinate system $(\tilde{r}, \theta, \tilde{z})$ with its origin located along the centreline of the initially cylindrical column and where $\tilde{z}$ is the axial coordinate measured along the column's axis, $\tilde{r}$ is the radial coordinate measured from that axis and θ is the usual angle measured around the symmetry axis $\tilde{r} = 0$. When subjected to axisymmetric shape perturbations of infinitesimal amplitude whose wavelength in the axial direction is given by $\tilde{\lambda}$, a quiescent cylindrical column of liquid undergoes capillary or Rayleigh–Plateau instability if $\tilde{\lambda} > 2\pi R$ or $\tilde{k}R < 1$ where $\tilde{k} = 2\pi/\tilde{\lambda}$ is the wavenumber (Plateau 1873; Rayleigh 1878; Michael 1981). In this paper, the capillary pinching of a surfactant-covered, quiescent liquid column is initiated by subjecting its surface $\tilde{S}(\tilde{t})$, where $\tilde{t}$ is time, at time $\tilde{t} = 0$ to a shape perturbation of sufficiently long wavelength but of arbitrary amplitude so that the column's profile is given by

$$\frac{\tilde{r}(\tilde{z}, \tilde{t} = 0)}{R} = \sqrt{1 - \frac{\epsilon^2}{2}} + \epsilon \cos \tilde{k}\tilde{z}. \tag{2.1}$$

When the disturbance amplitude is small, $\epsilon \ll 1$, (2.1) simplifies to $\tilde{r}(\tilde{z}, 0)/R = 1 + \epsilon \cos \tilde{k}\tilde{z}$. Two types of initial conditions are considered for surfactant concentration. In most cases, the jet is taken at $\tilde{t} = 0$ to be coated uniformly with surfactant at concentration $\tilde{\Gamma}_0$. In some cases, the concentration at the surface of a uniformly coated perfectly cylindrical column is perturbed in an analogous manner as its shape (see below).

The dynamics of the thinning and breakup of the jet is analysed by solving the transient free boundary problem consisting of the continuity and Navier–Stokes equations for fluid velocity $\tilde{\boldsymbol{v}}$ and pressure $\tilde{p}$ within the jet $\tilde{V}(\tilde{t})$ and the convection–diffusion equation for surfactant concentration $\tilde{\Gamma}$ on $\tilde{S}(\tilde{t})$:

$$\tilde{\boldsymbol{\nabla}} \cdot \tilde{\boldsymbol{v}} = 0 \quad \text{in } \tilde{V}(\tilde{t}), \tag{2.2}$$

$$\rho \left(\frac{\partial \tilde{\boldsymbol{v}}}{\partial \tilde{t}} + (\tilde{\boldsymbol{v}} \cdot \tilde{\boldsymbol{\nabla}}) \tilde{\boldsymbol{v}} \right) = \tilde{\boldsymbol{\nabla}} \cdot \tilde{\boldsymbol{T}} \quad \text{in } \tilde{V}(\tilde{t}), \tag{2.3}$$

$$\frac{\partial \tilde{\Gamma}}{\partial \tilde{t}} + \tilde{\boldsymbol{\nabla}}_s \cdot \left(\tilde{\Gamma} \tilde{\boldsymbol{v}} \right) = D_s \tilde{\boldsymbol{\nabla}}_s^2 \tilde{\Gamma} \quad \text{on } \tilde{S}(\tilde{t}). \tag{2.4}$$

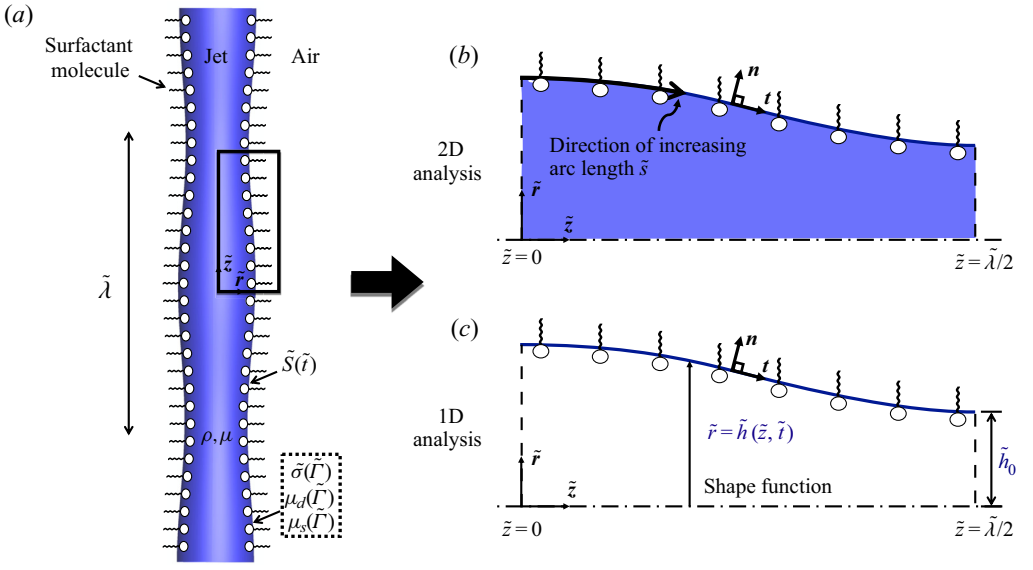

FIGURE 1. Definition sketch. (*a*) A liquid jet the surface $\tilde{S}(\tilde{t})$ of which is covered by a monolayer of an insoluble surfactant. To initiate capillary thinning and pinch-off, the surface of a perfectly cylindrical column of radius R is subjected at time $\tilde{t}=0$ to an axially periodic sinusoidal perturbation of wavelength $\tilde{\lambda}=2\pi/\tilde{k}$. (*b*) Domain of interest for 3DA or 2-D analysis. Here, the interface is parametrized by arc length $\tilde{s}$. (*c*) The 1-D domain. In both the 2-D and 1-D analyses, the axial extent of the domain is $0 \le z \le \tilde{\lambda}/2 = \pi/\tilde{k}$.

In (2.3), $\tilde{\boldsymbol{T}} = -\tilde{p}\boldsymbol{I} + \mu[\tilde{\boldsymbol{\nabla}}\tilde{\boldsymbol{v}} + (\tilde{\boldsymbol{\nabla}}\tilde{\boldsymbol{v}})^T]$ is the total stress tensor for a Newtonian fluid and $\boldsymbol{I}$ is the identity tensor. In (2.4), D_s is the surfactant diffusivity, $\tilde{\boldsymbol{\nabla}}_s \equiv \boldsymbol{I}^s \cdot \tilde{\boldsymbol{\nabla}}$ is the surface gradient operator and $\boldsymbol{I}^s \equiv \boldsymbol{I} - \boldsymbol{nn}$ is the surface identity tensor with $\boldsymbol{n}$ denoting the outward pointing unit normal to $\tilde{S}(\tilde{t})$.

As (2.2) and (2.3) are balances of mass and momentum conservation in the bulk $\tilde{V}(\tilde{t})$, the corresponding principles of mass and momentum conservation at the L–G interface $\tilde{S}(\tilde{t})$ are the kinematic and traction boundary conditions (Scriven 1960; Aris 2012). In the absence of bulk flow or mass transfer across the interface, the kinematic boundary condition is given by

$$\boldsymbol{n} \cdot (\tilde{\boldsymbol{v}} - \tilde{\boldsymbol{v}}_s) = 0, \tag{2.5}$$

where $\tilde{\boldsymbol{v}}_s$ is the velocity of points on the interface. If the surface of the jet is described as a compressible, two-dimensional Newtonian fluid, surface rheological effects that arise over and beyond the ordinary capillary and Marangoni stress effects obey the Boussinesq–Scriven constitutive equation (Scriven 1960). Then the traction or the stress-balance boundary condition at the free surface is given by

$$\begin{aligned}\boldsymbol{n} \cdot \tilde{\boldsymbol{T}} = {} & 2\tilde{\mathcal{H}}\tilde{\sigma}\boldsymbol{n} + \tilde{\boldsymbol{\nabla}}_s\tilde{\sigma} + 2\tilde{\mathcal{H}}\,(\mu_d - \mu_s)\left(\tilde{\boldsymbol{\nabla}}_s \cdot \tilde{\boldsymbol{v}}\right)\boldsymbol{n} \\ & + \tilde{\boldsymbol{\nabla}}_s\left[(\mu_d - \mu_s)\left(\tilde{\boldsymbol{\nabla}}_s \cdot \tilde{\boldsymbol{v}}\right)\right] + \tilde{\boldsymbol{\nabla}}_s \cdot \left[\mu_s\left(\tilde{\boldsymbol{\nabla}}_s\tilde{\boldsymbol{v}} \cdot \boldsymbol{I}^s + \boldsymbol{I}^s \cdot \left(\tilde{\boldsymbol{\nabla}}_s\tilde{\boldsymbol{v}}\right)^T\right)\right].\end{aligned} \tag{2.6}$$

Here, $2\tilde{\mathcal{H}} \equiv -\tilde{\boldsymbol{\nabla}} \cdot \boldsymbol{n}$ is twice mean curvature of the free surface. The first two terms on the right-hand side of (2.6) correspond to the capillary pressure and the Marangoni stress

due to surface tension gradients. The remaining terms account for surface rheological effects. Surface tension $\tilde{\sigma} = \tilde{\sigma}(\tilde{\Gamma})$ as well as the surface shear $\mu_s = \mu_s(\tilde{\Gamma})$ and the surface dilatational $\mu_d = \mu_d(\tilde{\Gamma})$ viscosities are all functions of surfactant concentration $\tilde{\Gamma}$ (see below).

Here, surface tension $\tilde{\sigma}$ is related to surfactant concentration $\tilde{\Gamma}$ via the Szyszkowski equation of state (Liao *et al.* 2006)

$$\tilde{\sigma} = \sigma_p + \tilde{\Gamma}_m R_g T \ln\left(1 - \frac{\tilde{\Gamma}}{\tilde{\Gamma}_m}\right), \tag{2.7}$$

where $\tilde{\Gamma}_m$ is the maximum packing density of surfactant, R_g is the gas constant and T is the absolute temperature. It will be shown below that the particular equation of state adopted to relate surface tension to surfactant concentration is immaterial as the pinch-off singularity is approached.

Since surface rheological effects arise when surfactants deform against themselves at interfaces, it accords with intuition that surface viscosities are functions of $\tilde{\Gamma}$. Although it is not known whether the functional form of $\mu_d(\tilde{\Gamma})$ is identical to that of $\mu_s(\tilde{\Gamma})$, the simplifying assumption is adopted in this paper that μ_d varies with $\tilde{\Gamma}$ in the same way as μ_s. Throughout the body of the paper, following recent works in the literature (Ponce-Torres *et al.* 2017), the surface viscosities are taken to vary linearly with $\tilde{\Gamma}$ with respect to a reference state

$$\mu_s = \mu_{sr}\tilde{\Gamma}/\tilde{\Gamma}_r, \quad \mu_d = \mu_{dr}\tilde{\Gamma}/\tilde{\Gamma}_r, \tag{2.8a,b}$$

where μ_{sr} and μ_{dr} are the reference surface viscosities at the reference surfactant concentration $\tilde{\Gamma}_r$. As shown in appendix A, some of the key results presented in this paper can be readily generalized so that they are independent of the constitutive equation used to relate surface viscosities to surfactant concentration.

Because the dynamics is axisymmetric about the $\tilde{z}$-axis, the shear stress and the radial velocity have to vanish at $\tilde{r} = 0$, *viz.* $\boldsymbol{e}_r \cdot \tilde{\boldsymbol{T}} \cdot \boldsymbol{e}_z = 0$ and $\tilde{u} \equiv \tilde{\boldsymbol{v}} \cdot \boldsymbol{e}_r = 0$ where $\boldsymbol{e}_r$ and $\boldsymbol{e}_z$ stand for the unit vectors in the radial and axial directions. On account of the periodicity of the imposed initial perturbation of the jet's surface, the problem only needs to be solved over an axial distance equal to one half of the wavelength of the imposed perturbation. Thus, along the two symmetry planes located at $\tilde{z} = 0$ and $\tilde{z} = \pi/\tilde{k} = \tilde{\lambda}/2$, both the shear stress and the axial velocity must vanish, *viz.* $\boldsymbol{e}_z \cdot \tilde{\boldsymbol{T}} \cdot \boldsymbol{e}_r = 0$ and $\tilde{v} \equiv \tilde{\boldsymbol{v}} \cdot \boldsymbol{e}_z = 0$. Also because of symmetry, surfactant concentration must obey $\boldsymbol{e}_z \cdot \tilde{\boldsymbol{\nabla}}_s \tilde{\Gamma} = 0$ at $\tilde{z} = 0$ and $\tilde{z} = \pi/\tilde{k}$.

2.2. *The 1-D slender-jet equations*

Since the jet radius is small relative to the length of the jet, a set of 1-D slender-jet or long-wavelength equations can be derived to analyse the dynamics of jet breakup. Thus, in this limit, both the axial velocity and the pressure to leading order are simply functions of the axial coordinate and time, *viz.* $\tilde{v} = \tilde{v}(\tilde{z}, \tilde{t})$ and $\tilde{p} = \tilde{p}(\tilde{z}, \tilde{t})$. From (2.2), it then follows that the radial velocity is small or to leading order of $O(\tilde{r})$, and is given by $\tilde{u}(\tilde{r}, \tilde{z}, \tilde{t}) = -(\tilde{r}/2)\partial\tilde{v}/\partial\tilde{z}$.

If the free-surface shape is represented as $\tilde{r} = \tilde{h}(\tilde{z}, \tilde{t})$ (figure 1), substitution of the leading-order expressions for $\tilde{u}$ and $\tilde{v}$ into (2.5) leads to the 1-D mass balance or the

kinematic boundary condition (KBC) that governs the transient evolution of the jet radius

$$\frac{\partial \tilde{h}}{\partial \tilde{t}} + \tilde{v}\frac{\partial \tilde{h}}{\partial \tilde{z}} + \frac{\tilde{h}}{2}\frac{\partial \tilde{v}}{\partial \tilde{z}} = 0. \tag{2.9}$$

Similarly, the 1-D convection–diffusion equation can be obtained from (2.4) (Ambravaneswaran & Basaran 1999) that governs the transient evolution of the surfactant concentration

$$\frac{\partial \tilde{\Gamma}}{\partial \tilde{t}} + \tilde{v}\frac{\partial \tilde{\Gamma}}{\partial \tilde{z}} + \frac{\tilde{\Gamma}}{2}\frac{\partial \tilde{v}}{\partial \tilde{z}} - \frac{D_s}{\tilde{h}}\frac{\partial}{\partial \tilde{z}}\left(\tilde{h}\frac{\partial \tilde{\Gamma}}{\partial \tilde{z}}\right) = 0. \tag{2.10}$$

To derive the 1-D momentum balance, a slightly different approach is adopted here than the one used by Eggers (1993) for jets with clean interfaces and Martínez-Calvo & Sevilla (2018) for surfactant-covered jets. The analysis is expedited by noting that the various components of the stress tensor are given by $\tilde{T}_{rr} \equiv \boldsymbol{e}_r \cdot \tilde{\boldsymbol{T}} \cdot \boldsymbol{e}_r$, $\tilde{T}_{rz} \equiv \boldsymbol{e}_r \cdot \tilde{\boldsymbol{T}} \cdot \boldsymbol{e}_z$, and $\tilde{T}_{zz} \equiv \boldsymbol{e}_z \cdot \tilde{\boldsymbol{T}} \cdot \boldsymbol{e}_z$. Although it is clear that the normal stresses $\tilde{T}_{zz}$ and $\tilde{T}_{rr}$ are uniform over the cross-section of the jet for a Newtonian fluid because $\tilde{T}_{zz} = -\tilde{p} + 2\mu(\partial \tilde{v}/\partial \tilde{z})$ and $\tilde{T}_{rr} = -\tilde{p} + 2\mu(\partial \tilde{u}/\partial \tilde{r}) = -\tilde{p} - \mu(\partial \tilde{v}/\partial \tilde{z})$, most of the following derivations can be generalized to situations where the stress tensor is arbitrary, e.g. when the fluid is viscoelastic, by assuming that the normal stresses are uniform in the cross-sectional plane (see, e.g. Bird, Armstrong & Hassager 1987) regardless of the constitutive equation used to describe the fluid's rheology. In general, without assuming that the jet is Newtonian, it is straightforward to show that at the L–G interface,

$$\boldsymbol{n} \cdot \tilde{\boldsymbol{T}} \cdot \boldsymbol{n} = \frac{1}{1 + (\partial \tilde{h}/\partial \tilde{z})^2}\left\{\tilde{T}_{rr} - 2\frac{\partial \tilde{h}}{\partial \tilde{z}}\tilde{T}_{rz} + \left(\frac{\partial \tilde{h}}{\partial \tilde{z}}\right)^2 \tilde{T}_{zz}\right\} \tag{2.11}$$

and

$$\boldsymbol{n} \cdot \tilde{\boldsymbol{T}} \cdot \boldsymbol{t} = \frac{1}{1 + (\partial \tilde{h}/\partial \tilde{z})^2}\left\{\frac{\partial \tilde{h}}{\partial \tilde{z}}\left(\tilde{T}_{rr} - \tilde{T}_{zz}\right) + \left[1 - \left(\frac{\partial \tilde{h}}{\partial \tilde{z}}\right)^2\right]\tilde{T}_{rz}\right\}, \tag{2.12}$$

where $\boldsymbol{t}$ is the unit tangent to the free surface.

Taking the dot or inner product of (2.6) with $\boldsymbol{n}$, using (2.11) and keeping the highest-order contributions leads to

$$\tilde{T}_{rr}|_{\tilde{r}=\tilde{h}(\tilde{z},\tilde{t})} = 2\tilde{\mathcal{H}}\tilde{\sigma} + \frac{1}{2\tilde{h}}\frac{\partial \tilde{v}}{\partial \tilde{z}}(3\mu_s - \mu_d). \tag{2.13}$$

Here, following Eggers (1993), the expression for the full curvature is retained in the capillary pressure term. As $\tilde{T}_{rr}$ does not vary with $\tilde{r}$, the expression (2.13) gives the radial normal stress throughout the cross-section of the jet. Taking the inner product of (2.6) with $\boldsymbol{t}$, using (2.12) and keeping the highest-order contributions leads to

$$\tilde{T}_{rz}|_{\tilde{r}=\tilde{h}(\tilde{z},\tilde{t})} = \frac{\partial \tilde{h}}{\partial \tilde{z}}\left(\tilde{T}_{zz} - \tilde{T}_{rr}\right) + \frac{\partial \tilde{\sigma}}{\partial \tilde{z}} + \frac{\partial}{\partial \tilde{z}}\left(\frac{3\mu_s + \mu_d}{2}\frac{\partial \tilde{v}}{\partial \tilde{z}}\right) + \frac{3\mu_s}{\tilde{h}}\frac{\partial \tilde{h}}{\partial \tilde{z}}\frac{\partial \tilde{v}}{\partial \tilde{z}}. \tag{2.14}$$

It is worth noting that, while $\tilde{v}$, $\tilde{T}_{rr}$ and $\tilde{T}_{zz}$ do not vary with $\tilde{r}$, $\tilde{T}_{rz}$ is a function of $\tilde{r}$; it vanishes at $\tilde{r} = 0$ because of axisymmetry and takes on the value given by (2.14) at the L–G interface.

Now that expressions have been obtained to leading order for all components of the stress tensor, the 1-D force balance or the momentum equation can be derived. Multiplying the $\tilde{z}$-component of (2.3) at leading order by $\tilde{r}$ and integrating over the cross-section of the jet yields

$$\rho\left(\frac{\partial \tilde{v}}{\partial \tilde{t}}+\tilde{v}\frac{\partial \tilde{v}}{\partial \tilde{z}}\right)=\frac{2}{\tilde{h}}\tilde{T}_{rz}|_{\tilde{r}=\tilde{h}(\tilde{z},\tilde{t})}+\frac{\partial \tilde{T}_{zz}}{\partial \tilde{z}}. \tag{2.15}$$

Equation (2.15) is valid irrespective of the rheology of the jet fluid. When ((2.13)–(2.14)) are substituted into (2.15), the 1-D momentum equation for a surfactant-covered jet is obtained

$$\begin{aligned}\rho\left(\frac{\partial \tilde{v}}{\partial \tilde{t}}+\tilde{v}\frac{\partial \tilde{v}}{\partial \tilde{z}}\right)=&\frac{\partial}{\partial \tilde{z}}\left(2\tilde{\mathcal{H}}\tilde{\sigma}\right)+\frac{2}{\tilde{h}}\frac{\partial \tilde{\sigma}}{\partial \tilde{z}}+\frac{1}{\tilde{h}^2}\frac{\partial}{\partial \tilde{z}}\left[\tilde{h}^2(\tilde{T}_{zz}-\tilde{T}_{rr})\right]\\&+\frac{1}{2\tilde{h}^2}\frac{\partial}{\partial \tilde{z}}\left(\mu_d\tilde{h}\frac{\partial \tilde{v}}{\partial \tilde{z}}\right)+\frac{9}{2\tilde{h}^2}\frac{\partial}{\partial \tilde{z}}\left(\mu_s\tilde{h}\frac{\partial \tilde{v}}{\partial \tilde{z}}\right).\end{aligned} \tag{2.16}$$

For a Newtonian fluid, $\tilde{T}_{zz}-\tilde{T}_{rr}=3\mu(\partial\tilde{v}/\partial\tilde{z})$ and the previous equation can be rewritten as

$$\begin{aligned}\rho\left(\frac{\partial \tilde{v}}{\partial \tilde{t}}+\tilde{v}\frac{\partial \tilde{v}}{\partial \tilde{z}}\right)=&\frac{\partial}{\partial \tilde{z}}\left(2\tilde{\mathcal{H}}\tilde{\sigma}\right)+\frac{2}{\tilde{h}}\frac{\partial \tilde{\sigma}}{\partial \tilde{z}}+\frac{3\mu}{\tilde{h}^2}\frac{\partial}{\partial \tilde{z}}\left(\tilde{h}^2\frac{\partial \tilde{v}}{\partial \tilde{z}}\right)\\&+\frac{1}{2\tilde{h}^2}\frac{\partial}{\partial \tilde{z}}\left(\mu_d\tilde{h}\frac{\partial \tilde{v}}{\partial \tilde{z}}\right)+\frac{9}{2\tilde{h}^2}\frac{\partial}{\partial \tilde{z}}\left(\mu_s\tilde{h}\frac{\partial \tilde{v}}{\partial \tilde{z}}\right).\end{aligned} \tag{2.17}$$

The various terms in the 1-D force balance correspond to inertial force, capillary force, Marangoni force, bulk viscous force and surface viscous forces associated with surface dilatation and shear deformation, respectively. It is noteworthy that in the slender-jet model, surface shear and dilatational viscous forces take on the same mathematical forms. Thus, we set $\mu_d=\mu_s$ for the sake of simplicity and only use μ_s in the rest of the paper.

As the 3DA equations, the slender-jet equations too are solved over half a wavelength of the imposed perturbation. In this limit, the boundary conditions on the dependent variables reduce to $\partial\tilde{h}/\partial\tilde{z}=0$, $\partial\tilde{\Gamma}/\partial\tilde{z}=0$ and $\tilde{v}=0$ at $\tilde{z}=0$ and $\tilde{z}=\pi/\tilde{k}=\tilde{\lambda}/2$.

3. Numerical and analytical solution methods

3.1. *The 3DA simulations*

The transient system of 3DA or 2-D ((2.2)–(2.4)) is solved numerically by means of a fully implicit, arbitrary Lagrangian–Eulerian method-of-lines (MOL) algorithm in which the Galerkin finite element method (G/FEM) is used for spatial discretization (Basaran 1992; Feng & Basaran 1994; Gresho & Sani 1998; Gockenbach 2006) and an adaptive, implicit finite difference method is employed for time integration (Gresho, Lee & Sani 1980; Patzek *et al.* 1991; Wilkes & Basaran 2001; Gockenbach 2006). As jet breakup is a free boundary problem that involves a highly deformable L–G interface, an elliptic mesh generation technique (Christodoulou & Scriven 1992) is employed to track the moving boundary and determine the radial and axial coordinates of each grid point in the moving, adaptive mesh simultaneously with the velocity and pressure unknowns in the jet as well as the free-surface profile and surfactant concentration along the interface. In the 3DA algorithm, the interface is parametrized in terms of arc length $\tilde{s}$ (see, e.g. Notz & Basaran

(2004) and figure 1). This parametrization, as opposed to using one where the interface shape is a single-valued function of the axial coordinate, coupled to the elliptic mesh generation algorithm allows simulation of the jet dynamics in which the interface may overturn (Notz & Basaran 2004). At each time step, the resulting system of nonlinear algebraic equations is solved iteratively using Newton's method where the Jacobian is computed analytically. Similar versions of the algorithm have already been used to analyse the breakup of jets, drops and filaments with and without surfactants (Notz & Basaran 2004; Liao *et al.* 2006; Kamat *et al.* 2018; Anthony *et al.* 2019; Anthony, Harris & Basaran 2020).

3.2. *The 1-D simulations*

The system of 1-D slender-jet equations ((2.9), (2.10), (2.17)) is solved numerically using a fully implicit MOL algorithm. The algorithm is based on the use of the G/FEM for spatial discretization and the same adaptive, implicit finite difference method as in the 3DA algorithm described above for time integration. Similar versions of this algorithm have already been used to solve 1-D evolution equations in analysing the breakup of liquid bridges and jets with and without surfactants and the dripping of leaky faucets (Zhang, Padgett & Basaran 1996; Ambravaneswaran & Basaran 1999; Ambravaneswaran, Phillips & Basaran 2000; Ambravaneswaran, Wilkes & Basaran 2002; Ambravaneswaran *et al.* 2004; Liao *et al.* 2006; Subramani *et al.* 2006; Wee *et al.* 2020).

3.3. *Similarity solutions*

In the vicinity of the space–time pinch-off singularity, similarity solutions can be constructed to the slender-jet equations. Such analyses are presented in the next section (§ 4). Solutions of the slender-jet equations that are obtained from simulations (§ 3.2) are used together with analyses carried out in similarity space to obtain in § 4 insights into pinch-off of jets in the absence and presence of surface rheological effects. Results of these analyses are then compared in § 5 with ones obtained from full 3DA simulations.

4. The 1-D results: similarity solutions and simulations

4.1. *Pinch-off without surface rheological effects*

In the absence of surfactants, Eggers (1993) has shown that as pinch-off is approached, jets with clean interfaces asymptotically thin according to

$$\frac{\tilde{h}_{min}}{l_\mu} = 0.0304\frac{\tilde{\tau}}{t_\mu}, \tag{4.1}$$

where $\tilde{\tau} \equiv \tilde{t}_b - \tilde{t}$ is time until pinch-off, and $\tilde{t}_b$ is the time at which pinch-off occurs. In the so-called IV scaling law given in (4.1), $\tilde{h}_{min}$ and $\tilde{\tau}$ are measured in units of or are normalized with the viscous length $l_\mu \equiv \mu^2/\rho\sigma_p$ and the viscous time $t_\mu \equiv \mu^3/\rho\sigma_p^2$, respectively (Eggers 1993; Castrejón-Pita *et al.* 2015). These characteristic scales in (4.1) are intimately tied to the dynamical balance between the three forces at play: capillary (surface tension), inertia and bulk viscous forces. In this case, the power-law exponent of unity that determines how the minimum radius scales with time measured from pinch-off, *viz.* $\tilde{h}_{min} \sim \tilde{\tau}$, and the amplitude of 0.0304 in the non-dimensional scaling law in (4.1), are universal, or observed irrespective of the experiment performed (Eggers 1993). Remarkably, when surfactants are present but surface rheological effects are neglected and

diffusion is weak, the exact same balance of forces is observed to hold (Timmermans & Lister 2002; Liao *et al.* 2006; McGough & Basaran 2006; Kamat *et al.* 2018) and it has been shown computationally by Liao *et al.* (2006), Kamat *et al.* (2018) and McGough & Basaran (2006) that (4.1) still describes the thinning of a surfactant-covered jet. To date, however, no self-similar analysis predicting this thinning rate has been carried out nor has an expression analogous to (4.1) for surfactant concentration been proposed. In the next few paragraphs, we provide these analyses in both the absence and presence of surface rheological effects.

In what follows, we use l_μ, t_μ and $\Gamma_p \equiv \sigma_p/R_gT$ as characteristic length, time and surfactant concentration scales to non-dimensionalize the problem. The characteristic velocity is then given by $l_\mu/t_\mu \equiv \sigma_p/\mu$, the visco-capillary velocity. Henceforward, a variable without a tilde represents the dimensionless counterpart of a variable with a tilde, e.g. $\tilde{h}_{min}$ is dimensional but $h_{min} \equiv \tilde{h}_{min}/l_\mu$ is dimensionless. Following Eggers (1993), we introduce the following (dimensionless) self-similar ansatz that the jet radius $h \equiv \tilde{h}/l_\mu$, axial velocity $v \equiv \tilde{v}/(\sigma_p/\mu)$ and surfactant concentration $\Gamma \equiv \tilde{\Gamma}/\Gamma_p$ have scaling forms given by

$$\left.\begin{aligned} h(z,t) &= \tau^{\alpha_h} H(\xi), \quad v(z,t) = \tau^{\alpha_v} V(\xi), \\ \Gamma(z,t) &= \tau^{\alpha_\Gamma} G(\xi), \quad \xi \equiv (z - z_b)/\tau^{\alpha_z}, \end{aligned}\right\} \tag{4.2}$$

where ξ is the similarity variable, z_b is the axial location where the jet will pinch off, α_h, α_v, α_Γ and α_z are scaling exponents and H, V and G are scaling functions. These relations are then substituted into the governing 1-D equations ((2.9), (2.10), and (2.17)) resulting in a set of ordinary differential equations (ODEs). By requiring that the ODEs in similarity space cannot depend on τ and using physical arguments, the scaling exponents can be deduced. The rates of jet thinning and surfactant depletion are then readily obtained by determination of the similarity functions to leading order.

When the 1-D convection–diffusion equation (2.10) is non-dimensionalized using the aforementioned scales, a single dimensionless group, the Péclet number *Pe*, emerges from the analysis

$$Pe \equiv \frac{(\sigma_p/\mu)l_\mu}{D_s} = \frac{\mu}{\rho D_s}. \tag{4.3}$$

If the solvent is water, $Pe \approx 10^3$ for common surfactants (Liao *et al.* 2006). For glycerol–water mixtures, the value of the Péclet number would yet be larger and range as $10^3 < Pe < 10^6$ (Liao *et al.* 2006). Therefore, we let $Pe \to \infty$ in the remainder of this section. We note that in this limit, the 1-D mass balance equation (2.9) for $\tilde{h}$ and the 1-D convection–diffusion equation (2.10) for $\tilde{\Gamma}$ become identical.

4.1.1. *Determination of scaling exponents*

The analysis when the interface is covered with surfactant is made more complicated than when the interface is clean by the presence of the Marangoni stress ($(2/h)(\partial\sigma/\partial z)$) and the nonlinearity of the Szyszkowski equation of state. Progress toward solving this problem is expedited by making the simple realization that the relationship between surfactant concentration Γ and surface tension σ is greatly simplified as breakup is approached. When the 1-D mass balance equation (or KBC) and the 1-D convection–diffusion equation (for $Pe \to \infty$), which are both spatially 1-D transient partial differential equations (PDEs), are cast onto similarity space, the requirement

that the resulting ODEs be independent of τ reveals from each of these equations that $\alpha_v = \alpha_z - 1$. With the use of this result, the 1-D mass balance equation and the 1-D convection–diffusion equation can be rewritten as

$$\frac{H'}{H} = -\frac{(1/2)V' - \alpha_h}{V + \alpha_z \xi}, \tag{4.4}$$

$$\frac{G'}{G} = -\frac{(1/2)V' - \alpha_\Gamma}{V + \alpha_z \xi}, \tag{4.5}$$

where prime denotes differentiation with respect to ξ. As a consequence of the boundedness of $V(\xi)$, there exists a point ξ_0 where the denominator on the right-hand sides of (4.4) and (4.5) vanish (Eggers 1993; Papageorgiou 1995). To ensure that the scaling function for the interface shape $H(\xi)$ and that for concentration $G(\xi)$ are well behaved, the numerators on the right-hand sides of these equations must also vanish at ξ_0, revealing that $(1/2)V'(\xi_0) = \alpha_h = \alpha_\Gamma$. Physically speaking, this regularity condition implies that, as pinch-off is approached ($\tau \to 0$) and the radius of the jet tends to zero ($\alpha_h > 0$), surfactant concentration must also tend to zero – a realization that accords with intuition in the limit of $Pe \to \infty$. Moreover, this fact allows the Szyszkowski equation of state to be linearized so that $\sigma = 1 - \Gamma$ as $\tau \to 0$.

Now that it has been shown that $\alpha_h = \alpha_\Gamma$ and that $\alpha_v = \alpha_z - 1$, two scaling exponents, say α_h and α_z, still remain unknown but can be uniquely determined by considering the dominant balance of forces in the momentum equation. When (4.2) is used in (2.17) (with the terms involving surface viscosity omitted), the latter can be written as

$$\alpha_z \xi V' + VV' - \alpha_v V = \frac{\tau^{2-2\alpha_z-\alpha_h}}{H^2}\left[H' - \tau^{\alpha_h}(HG)' + 3\tau^{\alpha_h - 1}(H^2 V')'\right]. \tag{4.6}$$

The left-hand side of (4.6) consists of the inertial terms. The terms on the right-hand side account for the capillary, Marangoni and bulk viscous forces, respectively. Using the physical requirement that the thread radius must decrease as pinch-off is approached ($\alpha_h > 0$), comparison of the Marangoni force with either capillary force or bulk viscous force immediately reveals that Marangoni force cannot enter the asymptotic dominant balance of forces. Balancing capillary and bulk viscous forces or requiring that the exponent of τ in the bulk viscous term vanish leads to $\alpha_h = 1$. The requirement that the ODE in similarity space be independent of τ or that capillary and bulk viscous forces balance inertia as $\tau \to 0$ then reveals that $\alpha_z = 1/2$. Therefore, in summary, the dominant balance of forces is that between inertial, capillary and bulk viscous forces as thread radius tends to zero and the scaling exponents are given by $\alpha_h = \alpha_\Gamma = 1$, $\alpha_z = 1/2$ and $\alpha_v = -1/2$. Recognition of the asymptotic insignificance of Marangoni stress and use of the scaling exponents that have just been determined then permits the set of ODEs governing the three scaling functions H, G, and V in similarity space to be rewritten as

$$\frac{H'}{H} = \frac{2 - V'}{2V + \xi}, \tag{4.7}$$

$$\frac{G'}{G} = \frac{2 - V'}{2V + \xi}, \tag{4.8}$$

$$\left(V\xi + V^2\right)' H^2 = 2H' + 6(H^2 V')'. \tag{4.9}$$

It should be noted that the scaling function G that enters the expression for the surfactant concentration in (4.2) is decoupled from the momentum equation (4.9) in similarity space.

This is a point that will be returned to and further elaborated on below. The physics dictates that the dynamics far from the pinch point must evolve much more slowly than that in vicinity of the singularity. Thus, solutions must be independent of τ as $z - z_b \to \pm\infty$. In similarity space, the far-field conditions on the scaling functions are hence given by

$$V(\xi) \sim \xi^{\alpha_v/\alpha_z} = \xi^{-1}, \tag{4.10}$$

$$H(\xi) \sim \xi^{\alpha_h/\alpha_z} = \xi^{2}, \tag{4.11}$$

$$G(\xi) \sim \xi^{\alpha_\Gamma/\alpha_z} = \xi^{2}, \tag{4.12}$$

as $|\xi| \to \infty$.

4.1.2. *Determination of thinning rate*

Now that the scaling exponents, the system of ODEs governing the scaling functions in similarity space, and the boundary conditions on the scaling functions have been established, the rate of thinning of the jet can be determined. To accomplish this goal, first the scaling functions are expressed in terms of a power series in ξ about the point ξ_0,

$$H(\xi) = \sum_{k=0}^{\infty} H_k(\xi - \xi_0)^k, \quad V(\xi) = \sum_{k=0}^{\infty} V_k(\xi - \xi_0)^k, \quad G(\xi) = \sum_{k=0}^{\infty} G_k(\xi - \xi_0)^k, \tag{4.13a–c}$$

and these series expansions are substituted into ((4.7)–(4.9)). The regularity condition, $V'(\xi_0) = 2$, allows the coefficients in the series expansions to be expressed in terms of recurrence relations

$$\begin{bmatrix} k(12H_0 + 1) & k(k+1)(3H_0^2) & 0 \\ 5k & H_0(k+1) & 0 \\ 0 & G_0(k+1) & 5k \end{bmatrix} \begin{bmatrix} H_k \\ V_{k+1} \\ G_k \end{bmatrix} = \begin{bmatrix} f_1(H_{k-1}, V_k) \\ f_2(H_{k-1}, V_k) \\ f_3(V_k, G_{k-1}) \end{bmatrix}. \tag{4.14}$$

The terms on the right-hand side, f_1, f_2 and f_3, depend on lower-order coefficients. The presence of zeros in the first two rows of the third column of the coefficient matrix in (4.14) is noteworthy and further demonstrates that the surfactant problem is decoupled from the other two equations as a result of the insignificance of Marangoni stress near pinch-off. Therefore, the similarity equations and far-field conditions for the scaling functions for the velocity and jet profile are identical in the presence and absence of surfactants. Hence, the rate of thinning of a surfactant-covered jet is expected to be the same as that in Eggers' case where the surface of the jet is clean or devoid of surfactant. Alternatively, one can proceed along the following lines presented below to determine the thinning rate. In order for a solution of these recurrence relations to exist, the determinant of the coefficient matrix must be non-zero for all k. While it is obvious from the governing equations, it is easy to see that the determinant vanishes independent of G_0 at values of H_0 given by

$$H_0^{sin}(n) = \frac{1}{(15n - 12)}, \quad n = 1, 2, 3, \ldots. \tag{4.15}$$

Although no similarity solution exists when $n = 1, 2, 3, \ldots$, Brenner, Lister & Stone (1996) in the absence of surfactants and Liao *et al.* (2006), McGough & Basaran (2006) and Kamat *et al.* (2018) in the absence of surface rheological effects have shown that the computed rate of thinning 0.0304 differs by less than a half of a per cent

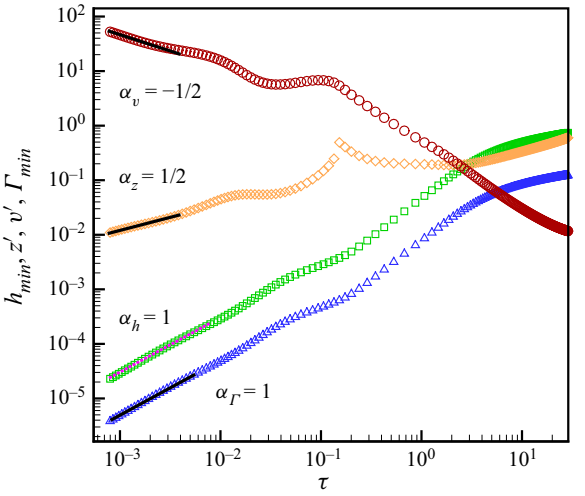

FIGURE 2. Transient evolution of minimum jet radius and surfactant concentration at that location and axial length and axial velocity predicted from 1-D simulations. Computed variation with τ of h_{min} (green square $\square$ symbols), $z' \equiv z_{1.04h_{min}} - z_{min}$ (orange diamond $\diamond$ symbols), $v' \equiv v_{1.04h_{min}}$ (red circle $\circ$ symbols) and $\Gamma_{min} \equiv \Gamma|_{h_{min}}$ (blue triangle $\triangle$ symbols) for a jet of $Pe = \infty$, $\Gamma_m = 0.3$ and $\Gamma_0 = 0.15$ in the absence of surface rheological effects. The solid black lines that are superimposed on the simulation results for h_{min}, z' and v' as $\tau \to 0$ correspond to theoretical scaling results and for which the indicated slopes are the power-law exponents predicted from theory. The pink dotted line, with the indicated slope of one, is Eggers' solution, $h_{min} = 0.0304\tau$, for either a jet with a clean interface (Eggers 1993) or a surfactant-covered jet without surface rheological effects (this paper).

from $H_0^{sin}(3) = 0.\overline{03}$. That this is indeed the case is demonstrated once again in figure 2 which shows results obtained from a 1-D simulation of the variation with time remaining until breakup τ of the thread's minimum radius h_{min}, the axial length scale $z' \equiv z_{\Lambda h_{min}} - z_{min}$ where $1 < \Lambda < 1.2$ and z_{min} and $z_{\Lambda h_{min}}$ stand for the axial location where the jet radius is a minimum and that where the jet radius equals Λ times h_{min}, respectively, the axial velocity scale $v' \equiv v_{\Lambda h_{min}}$ which is the value of the axial velocity evaluated at the axial location where the jet radius equals Λh_{min} and surfactant concentration where the thread's radius is a minimum $\Gamma_{min} \equiv \Gamma|_{h_{min}}$ in the absence of surface rheological effects. (We note that the scaling of the axial length can equivalently be determined from the scaling of the planar curvature.) Figure 2 makes plain that all dynamical variables – thread radius or radial length scale, axial length scale, axial velocity and surfactant concentration – exhibit the scaling behaviour that is discussed above and where it is shown that these variables have power-law dependencies on τ with the power-law or scaling exponents of 1, 1/2, $-1/2$ and 1, respectively.

4.1.3. *Determination of surfactant depletion rate*

While the analysis involving the recurrence relation presented in the previous subsection has resulted in the determination of H_0, which in turn has made it possible to predict from theory the variation of h_{min} with τ, that analysis has neither led to the value of G_0 nor determined how Γ_{min} varies with τ. Moreover, the universality and/or validity of (4.1) irrespective of the initial conditions that have been imposed have not yet been demonstrated. Progress towards this goal is made by recognizing that if $H(\xi)$ and $V(\xi)$

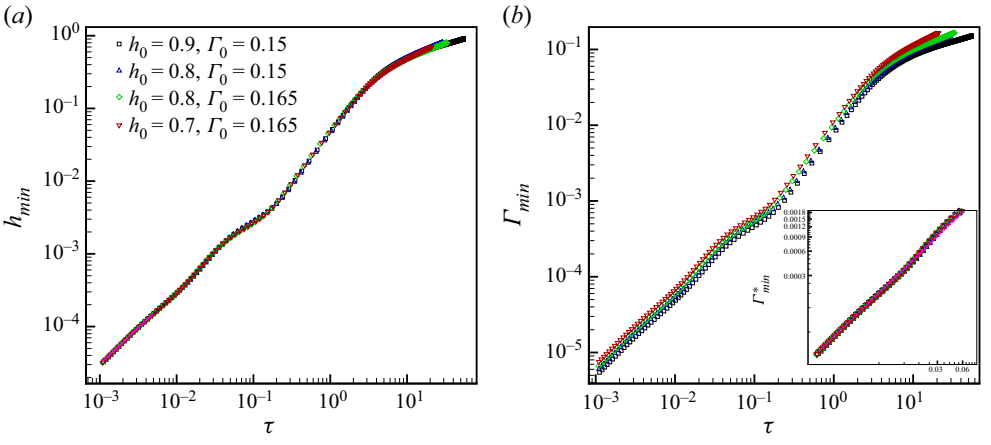

FIGURE 3. The 1-D simulation results of the computed variation with τ of (*a*) h_{min} and (*b*) Γ_{min} for jets of $Pe = \infty$ and $\Gamma_m = 0.3$ in the absence of surface rheological effects that are subjected to different initial conditions. The pink dotted line in (*a*) is that for which $h_{min} = 0.0304\tau$. All simulation data for h_{min} versus τ eventually collapse onto this line (Eggers' scaling law) irrespective of the initial conditions. By contrast, simulation data for Γ_{min} versus τ do not collapse onto a single line, which clearly illustrates that the evolution in time of Γ_{min} is dependent on initial conditions. Inset to figure 3(*b*) shows rescaled Γ_{min}, *viz.* $\Gamma^*_{min} \equiv \Gamma_{min}/c_0$, where $c_0 = \Gamma_0/h_0$. The collapse of the data obtained from simulations with different initial conditions onto one line $\Gamma^*_{min} = 0.0304\tau$, which is also denoted by a pink dotted line, makes plain that as $\tau \to 0$, $\Gamma_{min} = (0.0304\Gamma_0/h_0)\tau$.

are solutions to (4.7) and (4.9), then $G(\xi) = c_0 H(\xi)$, where c_0 is a constant, is a solution to (4.8). While the value of c_0 cannot be determined by scrutinizing the governing ODEs in similarity space, an examination of the transient PDEs in physical space reveals that because the 1-D mass balance equation and the 1-D convection–diffusion equation are identical in form, $c_0 = \Gamma_0/h_0$ where $h_0 = h_{min}(z_{min}, t = 0) \equiv h_{min}(L, 0)$ (figure 1) and $\Gamma_0 = \Gamma|_{h_0}$ (see appendix B). Figure 3(*a*) shows that (4.1) clearly describes the asymptotic variation of h_{min} with τ irrespective of the initial conditions but the variation of Γ_{min} with τ (figure 3*b*) clearly depends on Γ_0 and h_0. Moreover, by using the fact that $c_0 = \Gamma_0/h_0$, the variation of Γ_{min} with τ can be collapsed onto a single line given by $\Gamma^*_{min} \equiv \Gamma_{min}/c_0 = 0.0304\tau$ as shown in the inset to figure 3(*b*).

4.2. *Pinch-off with surface rheological effects (1D)*

4.2.1. *Determination of scaling exponents*

Armed with a thorough understanding of the asymptotic breakup dynamics in the absence of surface rheological effects when $Pe \to \infty$, we are now better positioned to begin to uncover how the physics of pinch-off is altered by their presence and also appreciate certain salient features and implications of the resulting dynamics. It is noteworthy to recall that surface rheological effects are accounted for by a single additional term in the 1-D momentum balance equation (2.17) compared to when they are absent. Therefore, the entire approach and analysis reported in the previous section prior to obtaining solutions, i.e. the self-similarity ansatz, the 1-D mass balance, the convection–diffusion equation, the linearization of the Szyszkowski equation, and the far-field conditions, with the exception of the 1-D momentum equation, apply unaltered

in the present situation. Thus, we borrow these earlier findings and exploit them to investigate how surface rheological effects alter the dominant force balance, thinning rate and surfactant depletion rate when $Pe \to \infty$.

Therefore, $\alpha_v = \alpha_z - 1$ and $\alpha_\Gamma = \alpha_h$ in the presence as well as absence of surface rheological effects, and the 1-D momentum equation with surface rheological effects in similarity space becomes

$$\alpha_z \xi V' + VV' - \alpha_v V = \frac{\tau^{2-2\alpha_z-\alpha_h}}{H^2}[H' - \tau^{\alpha_h}(HG)' + \tau^{\alpha_h-1}(3(H^2V')' + 5B_o(GHV')')], \tag{4.16}$$

where $B_o \equiv \mu_{sr}/\mu l_\mu$ is the Boussinesq–Scriven number and μ_{sr} is the reference surface viscosity ($\mu_{sr} \equiv \mu_s|_{\tilde{\Gamma}=\tilde{\Gamma}_p}$). Written in this form, it is clear that the term accounting for surface viscous effects (red) scales in exactly the same manner as the bulk viscous term. Thus, the forces entering the dominant balance are changed so that the balance is now between inertial, capillary, bulk viscous and surface viscous forces but the scaling exponents are unaltered so that $\alpha_h = \alpha_\Gamma = 1$, $\alpha_z = 1/2$ and $\alpha_v = -1/2$. Therefore, the power-law dependencies of the variation with τ of the jet radius, surfactant concentration, axial length and axial velocity are unaffected by surfactants that give rise to surface rheological effects compared to ones that do not. Thus, changes brought about by surface rheological effects are undetectable by considering scaling exponents alone and an analysis of the thinning rate is required. The modified rate of thinning can be determined by substituting the power series expansions given in (4.13*a–c*) into (4.16) which is first rewritten as

$$H^2(\xi V + V^2)' = 2H' + 6(H^2V')' + 10B_o(GHV')'. \tag{4.17}$$

Unlike the analysis in the absence of surface rheological effects, here, the momentum equation in similarity space governing the asymptotic thinning of the jet (4.17) includes effects brought on by surfactants.

4.2.2. *Determination of thinning rate*

When surface rheological effects are accounted for, the corresponding coefficient matrix that arises in the recurrence relations reported in § 4.1.2 in their absence can be shown to be given by

$$\begin{bmatrix} (12H_0 + 1 + 10B_oG_0)k & (3H_0 + 5B_oG_0)H_0k(k+1) & 10B_oH_0k \\ 5k & H_0(k+1) & 0 \\ 0 & G_0(k+1) & 5k \end{bmatrix}, \tag{4.18}$$

where the new terms that arise because of surface rheological effects have been highlighted in red. Here, the vanishing of the determinant of this matrix is clearly dependent upon G_0 as a result of the terms that are shown in red. In this case, the singular values of H_0 are given by

$$H_0^{sin}(n) = \frac{1}{(15n-12)} - \frac{5B_oG_0}{3}, \quad n = 1, 2, 3, \ldots. \tag{4.19}$$

Results of simulations highlighted in figure 4 when $B_o = 2/3$ and others in which the 1-D evolution equations have been solved in physical space show that when surface rheological

effects are accounted for, jets thin according to

$$h_{min} = \left(0.0304 - \frac{5B_oG_0}{3}\right)\tau. \tag{4.20}$$

This scaling law, shown by the black dashed line in figure 4, is extremely close to $h_{min} = H_0^{sin}(3)\tau$ but is markedly different from the scaling law given by (4.1) which is shown by the pink dotted line in figure 4. While figure 4 and the above analysis reveal that the power-law scaling of jet radius with τ is unaltered by surface viscosity, surface rheological effects profoundly affect the dynamics in that they reduce the asymptotic rate at which a jet thins: whereas the prefactor in the expression relating h_{min} to τ equals 0.0304 in the absence of surface rheological effects, the prefactor is reduced by $5B_oG_0/3$ in their presence. Using the same arguments as in § 4.1.3, it is clear that (4.20) can be rewritten as

$$h_{min} = \frac{0.0304}{\left(1 + \dfrac{5B_o\Gamma_0}{3h_0}\right)}\tau. \tag{4.21}$$

Written in this form, the term in the denominator that accounts for the reduction in the jet's thinning rate has a very simple physical interpretation. From the 1-D momentum equation (2.17), it can readily be appreciated that the ratio of surface viscous force to bulk viscous force locally scales as

$$\frac{\text{Surface viscous force}}{\text{Bulk viscous force}} \sim \frac{5}{3}\frac{\mu_s}{\mu\tilde{h}}, \tag{4.22}$$

where the term multiplying 5/3 can be thought of as a local Boussinesq–Scriven number. Therefore, it now becomes clear that $5B_oG_0/3H_0 = 5B_oc_0/3 = 5B_o\Gamma_0/3h_0$ represents the scale of the relative importance of surface viscous force to its bulk counterpart as $\tau \to 0$. Moreover, when written in the form given in (4.21), it is plain that the prefactor or amplitude in the scaling law is dependent on the initial conditions imposed on the jet. As a further check on the validity of this scaling law, it is shown in the inset to figure 5 that the thinning dynamics that arise for three different initial conditions all collapse onto one line the equation of which is given by $h^*_{min} \equiv h_{min}(1 + 5B_o\Gamma_0/3h_0) = 0.0304\tau$.

5. The 3DA results and discussion

In the previous section, analysis of the 1-D slender-jet equations by using theory and simulations in the limit of $Pe \to \infty$ has revealed the simple manner in which surface rheological effects act to slow the capillary thinning of a surfactant-covered jet. However, a number of real life complications may preclude the observation of dynamics that comports with the simple formulae given in that section. Among others, these complications include the following. For example, for a real system, Pe may be finite and surface viscosity may be a nonlinear function of $\tilde{\Gamma}$ (see appendix A). Also, the Eggers-like asymptotic regime of pinch-off reported earlier may not be observed until small length and time distances from the singularity are attained. Moreover, the value of h_{min} for which the dynamics would begin to follow the scaling laws given in that section may be smaller than the molecular length scale. Furthermore, as first shown by Castrejón-Pita *et al.* (2015) and later by Li & Sprittles (2016) during the capillary thinning of surfactant-free jets, the dominant balance of forces in the vicinity of the jet's minimum radius may change multiple times and hence the dynamics may traverse a number of intermediate scaling regimes (Eggers 2005)

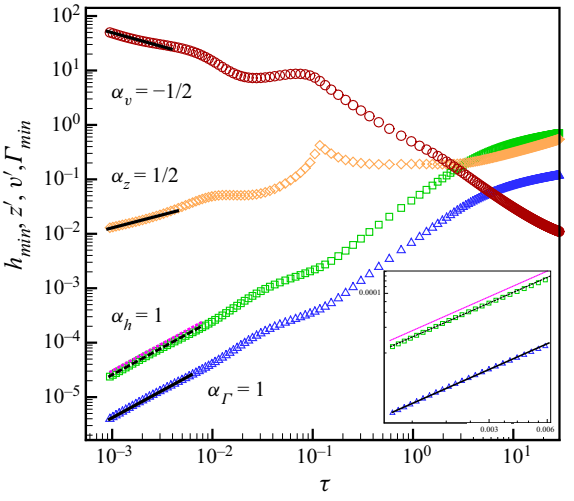

FIGURE 4. Transient evolution of minimum jet radius and surfactant concentration at that location and axial length and axial velocity predicted from 1-D simulations. Computed variation with τ of h_{min} (green square $\square$ symbols), $z' \equiv z_{1.04h_{min}} - z_{min}$ (orange diamond $\diamond$ symbols), $v' \equiv v_{1.04h_{min}}$ (red circle $\circ$ symbols) and $\Gamma_{min} \equiv \Gamma|_{h_{min}}$ (blue triangle $\triangle$ symbols) for a jet of $Pe = \infty$, $\Gamma_m = 0.3$ and $\Gamma_0 = 0.15$ in the presence of surface rheological effects ($B_o = 2/3$). The solid black lines that are superimposed on the simulation results for Γ_{min}, z' and v' as $\tau \to 0$ correspond to theoretical scaling results and for which the indicated slopes are the power-law exponents predicted from theory. The pink dotted line, with the indicated slope of unity, is Eggers' solution, $h_{min} = 0.0304\tau$, for a jet with a clean interface (Eggers 1993) or a surfactant-covered jet without surface rheological effects (this paper). The black dashed line, also of slope unity, is the plot of the equation given by $h_{min} = 0.0304\tau/(1 + 5B_o\Gamma_0/3h_0)$, i.e. (4.21). The inset shows a blow-up or zoomed-in view of both h_{min} and Γ_{min} versus τ and also helps make clear the difference between these two scaling laws.

before finally settling down in the final asymptotic regime of pinch-off as $\tau \to 0$. Kamat *et al.* (2018) have shown that such intermediate regimes are also encountered during the capillary thinning of a surfactant-covered jet albeit in the absence of surface rheological effects. Kamat *et al.* (2018) have further shown that the occurrence of the intermediate regimes that are encountered as a surfactant-laden jet approaches pinch-off is associated with a cascade of microthreads the occurrences of which are directly attributable to the action of Marangoni stresses.

Thus, in the remainder of this section, we analyse the capillary thinning and breakup of a surfactant-covered jet in the presence of surface rheological effects from simulations carried out by solving the full 3DA equations governing the dynamics of the jet. As in a real laboratory experiment that would be carried out with liquid jets or bridges, we take the unperturbed radius of the jet R, the inertio-capillary time scale $\sqrt{\rho R^3/\sigma_p}$, and the maximum packing density of surfactant $\tilde{\Gamma}_m$ as the characteristic length, time and surfactant concentration scales to non-dimensionalize the problem. To distinguish dimensionless variables using these new scales from ones used earlier, we use 'hats' so that hatted variables represent the dimensionless counterparts of variables with tildes, e.g. $\hat{h}_{min} \equiv \tilde{h}_{min}/R$ is dimensionless whereas $\tilde{h}_{min}$ is dimensional. With the introduction of these characteristic scales, it is found that the dynamics of surfactant-laden jets with surface rheological effects are governed by a number of dimensionless groups.

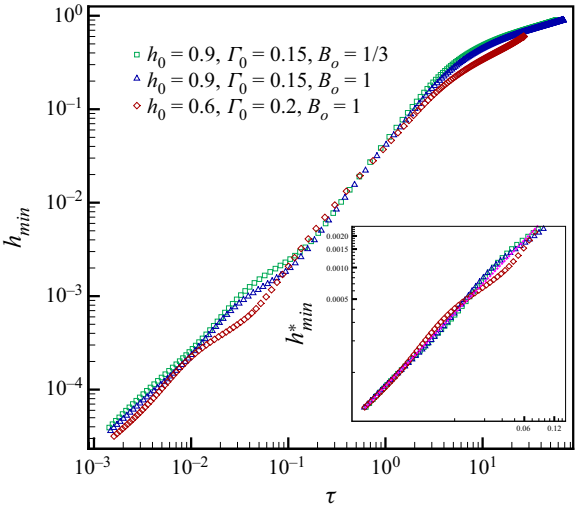

FIGURE 5. The 1-D simulation results on the computed variation with τ of h_{min} for a jet of $Pe = \infty$ and $\Gamma_m = 0.3$ in the presence of surface rheological effects ($B_o \neq 0$) that are subjected to different initial conditions. Unlike the situations in the absence of surface rheological effects, simulations reveal that when surface rheological effects are important the prefactor in the scaling law relating h_{min} and τ as $\tau \to 0$ is not only a function of B_o but also of the initial conditions ($c_0 = \Gamma_0/h_0$). The inset shows the variation of the rescaled minimum jet radius, $h^*_{min} \equiv h_{min}(1 + 5c_0B_o/3)$, with τ. The collapse shown in the inset of the data obtained from simulations with different initial conditions onto one line $h^*_{min} = 0.0304\tau$ (the pink dotted line) clearly reveals that surfactant-covered filaments in the presence of surface rheological effects do indeed thin according to (4.21).

They include: (a) the Ohnesorge number $Oh \equiv \mu/\sqrt{\rho R\sigma_p}$, and the dimensionless wavenumber and amplitude of the initial shape perturbation $\hat{k} \equiv \tilde{k}R$ and $\hat{\epsilon} \equiv \tilde{\epsilon}/R$ as in the case of jets with clean interfaces; the dimensionless initial surfactant coverage $\hat{\Gamma}_0 \equiv \tilde{\Gamma}_0/\tilde{\Gamma}_m$ and the surfactant strength parameter $\beta \equiv \tilde{\Gamma}_m R_g T/\sigma_p$ as with surfactant-covered jets without surface rheological effects; and the Boussinesq–Scriven number $B_s = B_{s0}(\hat{\Gamma}/\hat{\Gamma}_0)$ where $B_{s0} \equiv (\mu_s|_{\tilde{\Gamma}=\tilde{\Gamma}_0})/\mu R$.

5.1. *Scaling exponents*

Figure 6 shows the variation with time remaining until breakup $\hat{\tau}$ of the jet's minimum radius $\hat{h}_{min}$, the axial length scale $\hat{z}' \equiv \hat{z}_{1.09\hat{h}_{min}} - \hat{z}_{min}$, the axial velocity scale $\hat{v}' \equiv \hat{v}_{1.09\hat{h}_{min}}$ and surfactant concentration where jet radius is a minimum $\hat{\Gamma}_{min} \equiv \hat{\Gamma}_{\hat{h}_{min}}$ for two jets undergoing capillary thinning in the presence of surface rheological effects ($B_{s0} = 0.0143$). The two sets of simulation results are distinghuished by the fact in one $\hat{\Gamma}_0 = 0.55$ (figure 6a) and in the other $\hat{\Gamma}_0 = 0.5$ (figure 6b). We note that in contrast to the results shown in §§ 4.1 and 4.2, here Pe is large but finite ($Pe = 1000$).

Among others, two interesting features stand out in figure 6 compared to the 1-D results shown in figures 2–5: in figure 6(a,b), there exist several instants in time at which $\hat{v}'$ suddenly plummets and short periods of time where $\hat{\Gamma}_{min} \neq c\hat{h}_{min}$. These complex features, which are absent from the 1-D simulation results reported in §§ 4.1 and 4.2, are of course due to the existence of intermediate regimes and the repeated formation of microthreads, as

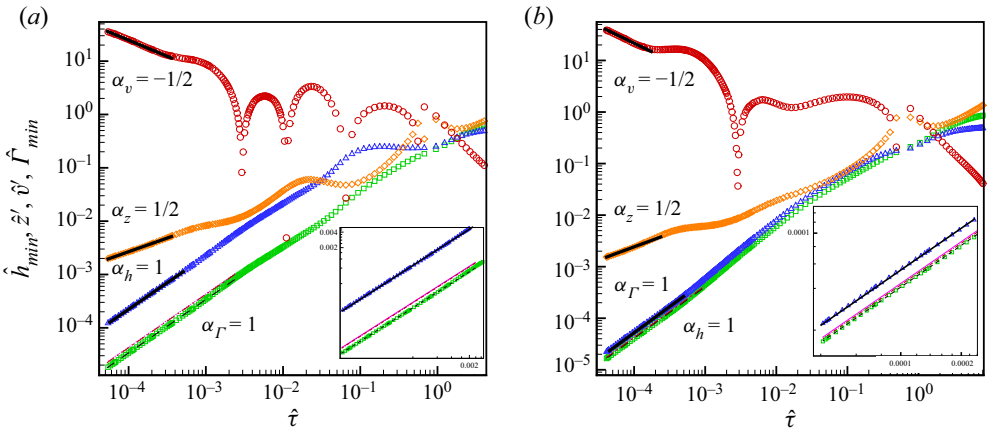

FIGURE 6. Transient evolution of minimum jet radius and surfactant concentration at that location and axial length and axial velocity predicted from 3DA simulations. (*a*) Computed variation with $\hat{\tau}$ of $\hat{h}_{min}$ (green square $\square$ symbols), $\hat{z}' \equiv \hat{z}_{1.09\hat{h}_{min}} - \hat{z}_{min}$ (orange diamond $\diamond$ symbols), $\hat{v}' \equiv \hat{v}'_{1.09\hat{h}_{min}}$ (red circle $\circ$ symbols) and $\hat{\Gamma}_{min}$ (blue triangle $\triangle$ symbols) for a jet of $Oh = 0.07$, $Pe = 1000$, $\beta = 0.3$, $\hat{\Gamma}_0 = 0.55$ and $B_{s0} = 0.0143$. (*b*) Same as (*a*) except $\hat{\Gamma}_0 = 0.5$. Insets: zoomed-in views of $\hat{h}_{min}$ and $\hat{\Gamma}_{min}$ versus $\hat{\tau}$ as $\hat{\tau} \to 0$. In both (*a*,*b*), the solid black lines that are superimposed on the simulation results for $\hat{\Gamma}_{min}$, $\hat{z}'$ and $\hat{v}'$ as $\tau \to 0$ correspond to theoretical scaling results and for which the indicated slopes are the power-law exponents predicted from theory. Also in both the main parts and the insets of (*a*,*b*), Eggers' solution, $\hat{h} = 0.0304\hat{\tau}/Oh$, is denoted by the pink dotted line of slope unity. Similarly, the new scaling law, $\hat{h} = [0.0304/Oh(1 + 5B_{s0}\hat{c}_0/3\hat{\Gamma}_0)]\hat{\tau}$, where $\hat{c}_0 \equiv \lim_{\hat{\tau}\to 0} \hat{\Gamma}_{min}/\hat{h}_{min}$, is denoted by the dashed black line of slope unity.

has already been reported in simulations and experiments by Kamat *et al.* (2018). Indeed, figure 7 shows the repeated formation of microthreads in (*a*) the presence and (*b*) absence of surface rheological effects during jet thinning. Although the number of microthreads in figure 7(*a*) – the number of times the stagnation zone approaches the axial location where thread radius is a minimum (Kamat *et al.* 2018) – is the same as in figure 7(*b*), the shape of the main thread is drastically different in the two cases. Furthermore, the number of instants at which the velocity plummets was found to be different in the presence and absence of surface rheological effects. The impact of this observation on thread profiles and what factors determine the number of times at which the velocity plummets remain open problems for future study. However, regardless of the differences that exist between 1-D and 3DA results for $\hat{\tau} > 10^{-3}$, figure 6(*a*,*b*) make plain that the dynamics asymptotically exhibits the same power-law scalings that are exhibited in the Eggers-like regime reported in the previous section. Thus, as pinch-off nears, the 3DA simulations reveal that the same dominant balance of forces exists here as in § 4.2.1 and that $\hat{h}_{min} \sim \hat{\tau}$, $\hat{v}' \sim \hat{\tau}^{-1/2}$, $\hat{z}' \sim \hat{\tau}^{1/2}$ and $\hat{\Gamma}_{min} \sim \hat{\tau}$ as $\hat{\tau} \to 0$.

5.2. *Thinning rate*

Although the power-law scalings obtained theoretically using the 1-D slender-jet equations are observed in the 3DA simulations (figure 6), the validity of the thinning rates predicted by (4.1) and (4.21) in the final asymptotic regime of pinch-off shown in figure 6 has yet to

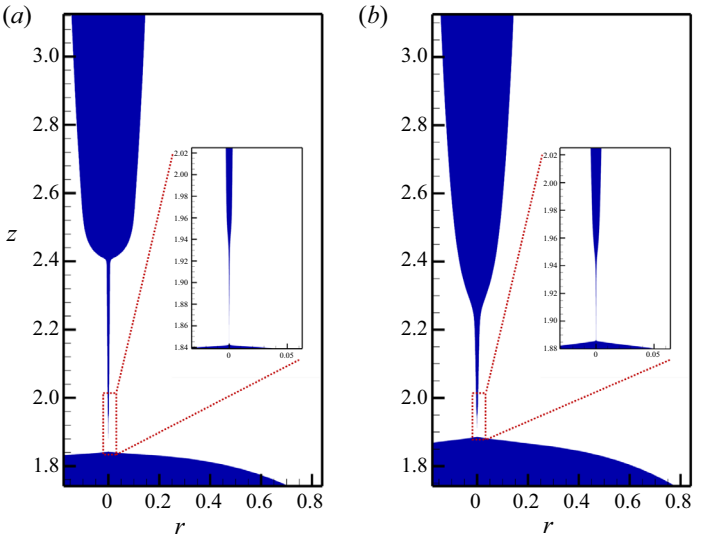

FIGURE 7. Profiles at the incipience of pinch-off of jets with and without surface rheological effects. (*a*) Zoomed-in views of microthreads at the instant in time when $t = 11.413$ for the same jet as in figure 6(*a*) and for which surface rheological effects are present. (*b*) Same as (*a*) except when surface rheological effects are absent or $B_{s0} = 0$ at the instant in time when $t = 11.357$. It should be noted that the parameter values in this case are identical to those used in figure 2 of the paper by Kamat *et al.* (2018).

be demonstrated. With the characteristic length and time scales used in this section, (4.1) and (4.21) can be rewritten as

$$\hat{h}_{min} = \frac{0.0304}{Oh}\hat{\tau}, \tag{5.1}$$

$$\hat{h}_{min} = \frac{0.0304}{Oh\left(1 + \dfrac{5B_{s0}}{3\hat{h}_0}\right)}\hat{\tau}. \tag{5.2}$$

It is easily seen from the insets to figure 6 that neither (5.1) (pink dotted line) nor (5.2) (red dashed-dotted line) accurately describes the thinning of surfactant-covered jets: the three lines corresponding to these two equations and the line corresponding to the simulation results all have the same slopes (of unity) but the amplitudes or prefactors in the expressions relating $\hat{h}_{min}$ to $\hat{\tau}$ evidently differ. While comparison of simulation data to the theoretical expressions clearly demonstrates that the thinning is slowed due to the effects of surface viscosity, the conditions implied in producing a closed form solution to thinning rate (see § 4.2.2) appear to be violated in the 3DA simulations. Specifically, the conditions under which the theory was developed cannot be naively applied in the present situation. This unexpected difficulty arises because in contrast to the results shown in figures 2 and 4, $\hat{\Gamma}_{min}$ is not linearly proportional to $\hat{h}_{min}$ during the early (figure 6*a*,*b*, $\hat{\tau} > 1$) and intermediate (figure 6*a*, $\hat{\tau} \approx 10^{-1}$) stages of thinning. Indeed, after the onset of the Rayleigh–Plateau instability, the jets whose dynamics are depicted in figure 6 do not immediately enter a final asymptotic Eggers-like regime. Thus, as shown in figure 6, these jets, as their surfactant-free counterparts and surfactant-covered ones without surface rheological effects, traverse a number of scaling regimes where the balance of forces

differs from that in the Eggers-like regime of § 4.2.2 and where the scaling exponents have different values than the ones in § 4.2.2. While the constant $\hat{c}_0$ relating $\hat{\Gamma}$ to $\hat{h}$ in the final asymptotic regime in an experiment or a 3DA simulation is no longer set by the initial conditions, its value can be readily determined from the 3DA simulations by computing the value of the ratio $\hat{\Gamma}_{min}/\hat{h}_{min}$ as $\hat{\tau} \to 0$. Therefore, the proper generalization of (5.2) is obtained by replacing the ratio $B_{s0}/\hat{h}_0$ by the ratio of the Boussinesq number and minimum jet radius at the onset of the final asymptotic regime. If the time at which the final asymptotic regime starts is denoted by $\hat{t}^*$,

$$\left.\frac{B_s}{\hat{h}_{min}}\right|_{\hat{t}=\hat{t}^*} = \frac{B_{s0}\dfrac{\hat{\Gamma}_{min}|_{\hat{t}=\hat{t}^*}}{\hat{\Gamma}_0}}{\hat{h}_{min}|_{\hat{t}=\hat{t}^*}} = \frac{B_{s0}}{\hat{\Gamma}_0}\frac{\hat{\Gamma}_{min}}{\hat{h}_{min}} = \frac{B_{s0}\hat{c}_0}{\hat{\Gamma}_0}, \tag{5.3}$$

where use has been made of the fact that in the final asymptotic regime, the ratio of $\hat{\Gamma}_{min}/\hat{h}_{min}$ is a constant. In conclusion, the proper generalization of (5.2) is then given by

$$\hat{h}_{min} = \frac{0.0304}{Oh\left(1 + \dfrac{5B_{s0}\hat{c}_0}{3\hat{\Gamma}_0}\right)}\hat{\tau}, \quad \text{where } \hat{c}_0 \equiv \lim_{\hat{\tau}\to 0}\left(\frac{\hat{\Gamma}_{min}}{\hat{h}_{min}}\right). \tag{5.4}$$

Since (5.4) applies as pinch-off nears, it can be rewritten so that it does not involve Oh by using $\hat{h}_{min} = \tilde{h}_{min}/R = (\tilde{h}_{min}/l_\mu)Oh^2 = h_{min}Oh^2$ and $\hat{\tau} = \tilde{\tau}/t_c = (\tilde{\tau}/t_\mu)Oh^3 = \tau Oh^3$:

$$h_{min} = \frac{0.0304}{1 + \dfrac{5B_{s0}\hat{c}_0}{3\hat{\Gamma}_0}}\tau, \tag{5.5}$$

where $\hat{c}_0 \equiv \hat{\Gamma}_{min}/\hat{h}_{min}$ as $\tau \to 0$.

The generalized approach and the result stated in (5.4) have been found to be valid for every 1-D and 3DA simulation in which the spatially 1-D and 3DA transient PDEs, i.e. the 1-D and 3DA evolution equations, are solved, including the simulation results reported in this paper. Investigation from 3DA simulations of the functional dependence of $\hat{c}_0$ upon the set of parameters governing the problem is left as an open problem.

6. Conclusions

In this paper, we have examined the capillary thinning and pinch-off of surfactant-covered Newtonian jets when surfactant convection is dominant over surfactant diffusion, *viz.* $Pe \gg 1$, along the interface. The dynamics close to the space–time pinch-off singularity has been analysed theoretically in the limit of $Pe = \infty$ and by simulation. In the theoretical approach, advantage has been taken of the fact that jet profiles in the vicinity of the pinch-off singularity are slender and hence a set of 1-D slender-jet equations have been used to probe the fluid dynamics. In the theoretical approach, the separation of length and time scales near the singularity from those in the bulk of the jet has been exploited to obtain self-similar solutions for the jet profile $h \equiv \tilde{h}/l_\mu$, surfactant concentration $\Gamma \equiv \tilde{\Gamma}/\Gamma_p$ and axial velocity $v' \equiv \tilde{v}'/(\sigma_p/\mu)$. As such, the asymptotic solutions presented in this paper are the counterparts of Eggers's inertial–viscous solution (Eggers 1993) for jets with clean interfaces.

In the absence as well as the presence of surface rheological effects, the similarity solutions have been shown to have a scaling form in which the dependence of jet radius h, surfactant concentration Γ, axial length z' and axial velocity v' on time remaining until pinch-off τ have power-law dependencies that are governed by universal scaling exponents, *viz.*

$$h \sim \tau, \quad \Gamma \sim \tau, \quad z' \sim \tau^{1/2}, \quad v' \sim \tau^{-1/2}. \tag{6.1a–d}$$

In the absence of surface rheological effects, as $\tau \to 0$, the jet thins as if surfactants are not present and the expression relating jet radius, and hence the minimum neck radius h_{min}, to τ is identical to that obtained by Eggers (1993). In this case, the surfactant concentration at the location where jet radius is a minimum Γ_{min} is proportional to h_{min}. Moreover, in this case while the asymptotic variation of h_{min} with τ is independent of initial conditions, these conditions do enter the asymptotic relation between Γ_{min} and τ.

In the presence of surface rheological effects, the power-law scalings are unchanged and h, Γ, z' and v' scale with time measured from pinch-off τ as in (6.1*a–d*). In this case, however, the asymptotic rate of thinning is reduced by a factor proportional to the ratio of surface to bulk viscous stresses at the onset of the asymptotic thinning regime.

In the absence of surface rheological effects, inertial, capillary and bulk viscous forces balance as the jet tends toward pinch-off. In the presence of surface rheological effects, however, inertial, capillary, bulk viscous and surface viscous forces balance as the jet nears pinch-off. In both cases, Marangoni stresses do not contribute to the dominant balance of forces near pinch-off. Also in both cases, $h_{min} \sim \Gamma_{min} \sim \tau$ and the ratio of Γ_{min} to h_{min} remains constant as $\tau \to 0$. A remarkable but counterintuitive feature of the physics when surface rheological effects are present is that surface viscosities can be important even when surfactants are swept away from the pinching zone and, consequently, surface viscosities vanish. This observation, however, can be readily rationalized because the ratio of the jet's surface area to its volume near the pinch point scales as $1/h_{min}$ which grows without bound as the jet's minimum radius h_{min} tends to zero. Since the thinning rate is a function of the surface viscosity and Marangoni stresses are negligible as pinch-off is approached, the results presented in this study on jet breakup can be used to develop a feasible and robust probeless method for measuring surface viscosity.

Pioneering studies of pinch-off of liquid jets of pure Newtonian fluids had uncovered the existence of three scaling regimes of breakup: an inertial–viscous regime where capillary, inertial and viscous forces balance (Eggers 1993), a viscous regime where capillary and viscous forces balance (Papageorgiou 1995) and an inertial regime where capillary and inertial forces balance (Chen & Steen 1997; Day, Hinch & Lister 1998). In the aftermath of the discovery of scaling laws governing pinch-off of jets with clean interfaces, it was realized that the viscous and inertial regimes can only be initial regimes of capillary thinning for slightly and highly viscous fluids and that the asymptotic regime of pinch-off must always involve all three forces (Lister & Stone 1998; Basaran 2002; Eggers 2005). In other words, when $Oh \ll 1$, a jet must undergo a transition from the inertial to the inertial–viscous regime as $\tau \to 0$. Similarly, when $Oh \gg 1$, a jet must undergo a transition from the viscous to the inertial–viscous regime as $\tau \to 0$. A jet of $Oh \approx 1$ can, however, remain in the inertial–viscous regime all the way until breakup. Subsequently, it was shown that the fluid dynamics of capillary thinning is in fact much more complicated than these earlier studies had implied (Castrejón-Pita *et al.* 2015; Li & Sprittles 2016). Indeed, a jet of $Oh \ll 1$ can undergo a transition from an initial inertial regime to an intermediate viscous regime and then eventually transition to the inertial–viscous regime as the jet tends toward pinch-off. By contrast, a jet of $Oh \gg 1$ can undergo transitions from an initial viscous to an intermediate inertial regime and then transition back to a second

intermediate viscous regime before finally transitioning to the final inertial–viscous regime as $\tau \to 0$. The existence of multiple intermediate or transient scaling regimes has already been demonstrated for surfactant-covered jets in the absence of surface rheological effects (Kamat *et al.* 2018). A short foray into the existence of such complexity is presented in this paper in figure 6. A fruitful avenue of future research would entail a more detailed examination of this complexity and transitions between different scaling regimes through 3DA simulations and experiments. This promising avenue of research is left as an open problem in fluid mechanics of capillary pinch-off. Another fascinating extension of the present study that would have far reaching practical implications would involve examination of the role of surface viscous stresses in determining drop sizes and drop size distributions in fields as diverse as ink jet printing (Basaran *et al.* 2013; Castrejon-Pita *et al.* 2013) and sprays and/or atomization (Hilz & Vermeer 2013; Kooij *et al.* 2018).

Acknowledgements

The authors thank the Purdue Process Safety and Assurance Center (P2SAC) for financial support.

Declaration of interests

The authors report no conflict of interest.

Appendix A. General constitutive equation for surface viscosity

Rather than assuming the linear relation that $B_s = B_{s0}\hat{\Gamma}/\hat{\Gamma}_0$, one can take $B_s = B_{s0}f(\hat{\Gamma})$ where the function f is such that $f(\hat{\Gamma}_0) = 1$ and $f(0) = 0$. A Taylor series expansion of $f(\hat{\Gamma})$ about $\hat{\Gamma} = 0$ then reveals that

$$f(\hat{\Gamma}) = f(0) + \left.\frac{\mathrm{d}f}{\mathrm{d}\hat{\Gamma}}\right|_{\hat{\Gamma}=0} \hat{\Gamma} + O(\hat{\Gamma}^2) = f'(0)\hat{\Gamma} + \ldots. \tag{A 1}$$

Thus, $B_s = B_{s0}f'(0)\hat{\Gamma}$ as $\hat{\Gamma} \to 0$ in the pinching region. Hence, the generalization of the results given earlier but now without any dependence whatsoever on a particular constitutive relation can be obtained by replacing $B_{s0}/\hat{\Gamma}_0$ by $B_{s0}f'(0)$ in those formulae. Consequently, the generalization of (5.4) then becomes

$$\hat{h}_{min} = \frac{0.0304}{Oh\left(1 + \dfrac{5B_{s0}f'(0)\hat{c}_0}{3}\right)}\hat{\tau}, \tag{A 2}$$

where $5B_{s0}f'(0)\hat{c}_0/3$ represents the relative importance of surface viscous force to its bulk counterpart to leading order as $\tau \to 0$.

In order to show how (A 2) is applied, we take the Boussinesq–Scriven number to vary linearly with surface pressure $\tilde{\Pi} = \sigma_p - \tilde{\sigma}$, *viz.* $B_s = B_{s0}\Pi/\Pi_0$, where Π_0 is the surface pressure at $\hat{\Gamma} = \hat{\Gamma}_0$. In this example, $f(\hat{\Gamma}) = \Pi/\Pi_0$ and $f'(0) = -1/\ln(1 - \hat{\Gamma}_0)$ where $f'(0)$ has been obtained from the Szyszkowski equation of state. As shown in figure 8, scaling exponents for minimum jet radius, axial length, axial velocity and surfactant concentration at the location where jet radius is minimum obtained from 3DA simulations by using a nonlinear constitutive equation for surface viscosity perfectly

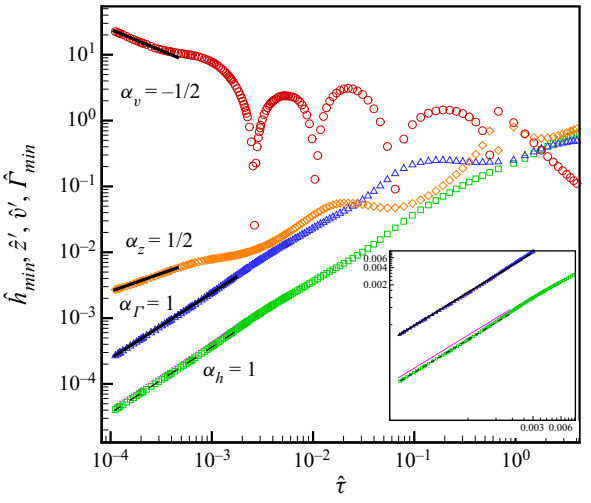

FIGURE 8. Results obtained from 3DA simulations using a nonlinear constitutive equation for surface viscosity: computed variation with $\hat{\tau}$ of $\hat{h}_{min}$ (green square $\square$ symbols), $\hat{z}' \equiv \hat{z}_{1.09\hat{h}_{min}} - \hat{z}_{min}$ (orange diamond $\diamond$ symbols), $\hat{v}' \equiv \hat{v}'_{1.09\hat{h}_{min}}$ (red circle $\circ$ symbols) and $\hat{\Gamma}_{min}$ (blue triangle $\triangle$ symbols) for a jet of $Oh = 0.07$, $Pe = 1000$, $\beta = 0.3$, $\hat{\Gamma}_0 = 0.55$ and $B_{s0} = 0.0143$. The solid black lines that are superimposed on the simulation results for $\hat{\Gamma}_{min}$, $\hat{z}'$ and $\hat{v}'$ as $\hat{\tau} \to 0$ correspond to theoretical scaling results and for which the indicated slopes are the power-law exponents predicted from theory. Inset: zoomed-in view of $\hat{h}_{min}$ and $\hat{\Gamma}_{min}$ versus $\hat{\tau}$ as $\hat{\tau} \to 0$. Eggers' solution, $\hat{h} = 0.0304\hat{\tau}/Oh$, is denoted by the pink dotted line. The new scaling law, $\hat{h} = [0.0304/Oh(1 + 5B_{s0}f'(0)\hat{c}_0/3)]\hat{\tau}$, where $\hat{c}_0 \equiv \lim_{\hat{\tau}\to 0} \hat{\Gamma}_{min}/\hat{h}_{min}$, is denoted by the dashed black line.

match the theoretical predictions reported earlier in which surface viscosity is assumed to vary linearly with surfactant concentration. Therefore, even when a nonlinear constitutive equation is used, asymptotically inertial, bulk viscous, surface viscous and capillary forces balance but Marangoni force is subdominant, and the rate of filament thinning, while it deviates from Eggers' scaling law for clean interfaces, proceeds according to (A 2).

Appendix B. Initial surfactant concentration profile

The 1-D mass balance (2.9) and 1-D convection–diffusion (2.10) are subjected to the same homogeneous Neumann boundary conditions at the two ends of the domain. Moreover, in the limit as Péclet number Pe or the relative importance of convection to diffusion grows without bound, the 1-D mass balance equation (2.9) and 1-D convection–diffusion equation (2.10) become identical in form

$$\frac{\partial h}{\partial t} + v\frac{\partial h}{\partial z} + \frac{h}{2}\frac{\partial v}{\partial z} = 0, \quad \frac{\partial \Gamma}{\partial t} + v\frac{\partial \Gamma}{\partial z} + \frac{\Gamma}{2}\frac{\partial v}{\partial z} = 0. \tag{B 1a,b}$$

(In this appendix, we omit the tildes from all variables for simplicity.) If we then write

$$\Gamma(z, t) = c(z, t)\, h(z, t), \tag{B 2}$$

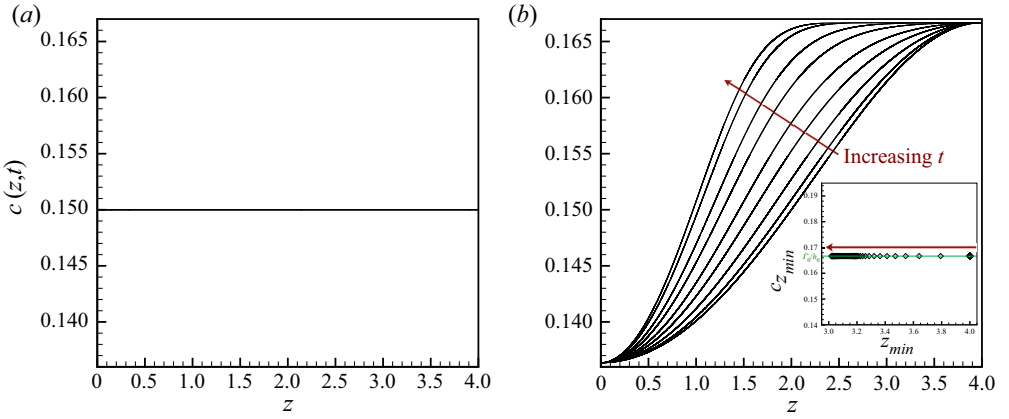

FIGURE 9. Time evolution of $c(z, t)$ for jets of $Pe = \infty$, $\Gamma_m = 0.3$, $\lambda = 8$ and $h_0 = 0.9$ subjected to different initial conditions on surfactant concentration. (*a*) Surfactant concentration is initially taken to be proportional to the initial shape profile $h(z, t = 0)$, *viz.* $\Gamma(z, t = 0) = c_0 h(z, t = 0)$. Here, $c_0 = 0.15$. Because $\mathrm{D}c/\mathrm{D}t = 0$, $c(z, t)$ must be spatially uniform and temporally constant for all time, *viz.* $c(z, t) \equiv c_0$. Thus profiles of $c(z, t)$ at different times determined from direct numerical simulations collapse onto one flat line, $c = c_0 = 0.15$, as shown in the figure. (*b*) The jet is initially uniformly coated with surfactant at concentration $\Gamma_0 = 0.15$. The different curves show the evolution in time of $c(z, t)$ and highlight the growing size of the axial extent where the profile of c is flat. Inset: variation of the computed value of $c(z = z_{min}, t)$ (denoted by diamond $\diamond$ symbols) with z_{min} where z_{min} denotes the axial location where the thread radius is minimum. The green flat line in the inset corresponds to Γ_0/h_0, which clearly shows $\lim_{\tau \to 0} \Gamma_{min}/h_{min} = \Gamma_0/h_0$. The red arrows in both the main figure and the inset indicate the direction of increasing time.

and substitute the previous product solution into either of the two equations in (B 1), it is found that

$$\frac{\mathrm{D}c}{\mathrm{D}t} = \frac{\partial c}{\partial t} + v\frac{\partial c}{\partial z} = 0. \tag{B 3}$$

The initial condition on the jet radius, $h(z, 0)$, is such that it corresponds to a sinusoidal deformation of the interface (2.1). If we take the initial condition on the surfactant concentration, $\Gamma(z, 0)$, to be of the same functional form such that $\Gamma(z, 0) = c_0 h(z, 0)$, where c_0 is a constant, it then follows from (B 3) that $c(z, t) = c_0$ for all time. The correctness of this statement is also confirmed by results of direct numerical simulations that are shown in figure 9(*a*). Thus, in this situation, $\Gamma(z, t) = c_0 h(z, t)$, a result that is used in the asymptotic analyses carried out in the paper.

It is also common in computational studies to impose the initial condition that the surfactant concentration is initially uniform, *viz.* $\Gamma(z, 0) = \Gamma_0 =$ constant, albeit the fact that the interface is deformed at that instant. In this case, $c(z, t)$ is no longer spatially uniform and temporally constant but instead evolves according to $\mathrm{D}c/\mathrm{D}t = 0$. Thus, because the material derivative of c is zero, the value of c remains constant following the motion of any material point. Since $c(z, t = 0)$ is continuous over $z \in [0, L]$, where $L \equiv \lambda/2 = \pi/k$, $c(z, t = 0)$ is bounded with $c(0, t = 0) \leq c(z, t = 0) \leq c(L, t = 0)$, *viz.* $c(0, 0) \leq c(z, 0) \leq c(L, 0)$, because $h(0, 0) \geq h(z, 0) \geq h(L, 0)$. Realization of boundedness and the imposed initial conditions on $\Gamma(z, t)$ and $h(z, t)$ and the equation governing $c(z, t)$ reveals that $c(0, 0) \leq c(z, t) \leq c(L, 0)$. At early times, the minimum in the jet radius is located at $z = L$. As the jet continues to thin, the fluid accelerates

as it flows from the neck, where pressure is highest, toward the swell ($z = 0$), where pressure is lowest. Consequently, $v < 0$ for $z \in (0, L)$ at early times. Since the imposed initial conditions on h and Γ give rise to positive $\partial c/\partial z$, c must increase as $\partial c/\partial t = -v\,\partial c/\partial z > 0$. Since $c(z, t)$ is bounded, its value anywhere can at most rise to its maximum value at the initial instant, $c(L, 0) = \Gamma_0/h_0$. Once the local value of c reaches its maximum value, the value of c there is maintained to be $c(L, 0)$ for all time as $c(z, t)$ develops flat profile over values of z where $c(z, t) = c(L, 0)$. Because of inertia, the location of minimum neck radius migrates from the end of the domain ($z = L$) to its interior (Eggers 1993; Castrejón-Pita *et al.* 2015). As shown by Castrejón-Pita *et al.* (2015), the occurrence of this new axial location $0 \ll z < L$ for the minimum value of jet radius gives rise to a new stagnation zone in the vicinity of which the flow has slowed down considerably and even reversed. At first sight, it might seem that $c(z, t)$ can decrease from its maximum value over the region where flow is reversed ($v > 0$). However, because $\partial c/\partial z = 0$ over this region, $c(z, t)$ remains fixed there equal to $c(L, 0)$. Therefore, we expect that $c(z = z_{min}, t) = c(L, 0) = \Gamma_0/h_0$ for all time, where z_{min} is the location where thread radius is minimum. The correctness of this assertion has been confirmed by direct numerical simulations. One example of such a simulation-based confirmation is shown in the inset to figure 9(*b*).

REFERENCES

AHMADI, M. A., GALEDARZADEH, M. & SHADIZADEH, S. R. 2015 Wettability alteration in carbonate rocks by implementing new derived natural surfactant: enhanced oil recovery applications. *Trans. Porus Media* **106** (3), 645–667.

AMBRAVANESWARAN, B. & BASARAN, O. A. 1999 Effects of insoluble surfactants on the nonlinear deformation and breakup of stretching liquid bridges. *Phys. Fluids* **11** (5), 997–1015.

AMBRAVANESWARAN, B., PHILLIPS, S. D. & BASARAN, O. A. 2000 Theoretical analysis of a dripping faucet. *Phys. Rev. Lett.* **85** (25), 5332–5335.

AMBRAVANESWARAN, B., SUBRAMANI, H. J., PHILLIPS, S. D. & BASARAN, O. A. 2004 Dripping-jetting transitions in a dripping faucet. *Phys. Rev. Lett.* **93** (3), 034501.

AMBRAVANESWARAN, B., WILKES, E. D. & BASARAN, O. A. 2002 Drop formation from a capillary tube: comparison of one-dimensional and two-dimensional analyses and occurrence of satellite drops. *Phys. Fluids* **14** (8), 2606–2621.

ANTHONY, C. R., HARRIS, M. T. & BASARAN, O. A. 2020 Initial regime of drop coalescence. *Phys. Rev. Fluids* **5** (3), 033608.

ANTHONY, C. R., KAMAT, P. M., HARRIS, M. T. & BASARAN, O. A. 2019 Dynamics of contracting filaments. *Phys. Rev. Fluids* **4** (9), 093601.

ARIS, R. 2012 *Vectors, Tensors and the Basic Equations of Fluid Mechanics*. Courier Corporation.

BASARAN, O. A. 1992 Nonlinear oscillations of viscous liquid drops. *J. Fluid Mech.* **241**, 169–198.

BASARAN, O. A. 2002 Small-scale free surface flows with breakup: drop formation and emerging applications. *AIChE J.* **48** (9), 1842–1848.

BASARAN, O. A., GAO, H. & BHAT, P. P. 2013 Nonstandard inkjets. *Annu. Rev. Fluid Mech.* **45**, 85–113.

BERG, J. C. 2010 *An introduction to Interfaces & Colloids: The Bridge to Nanoscience*. World Scientific.

BIRD, R. B., ARMSTRONG, R. C. & HASSAGER, O. 1987 *Dynamics of Polymeric Liquids, Volume 1: Fluid Mechanics*, 2nd edn. Wiley.

BRENNER, M. P., LISTER, J. R. & STONE, H. A. 1996 Pinching threads, singularities and the number 0.0304 . . . *Phys. Fluids* **8** (11), 2827–2836.

CASTREJON-PITA, J. R., BAXTER, W. R. S., MORGAN, J., TEMPLE, S., MARTIN, G. D. & HUTCHINGS, I. M. 2013 Future, opportunities and challenges of inkjet technologies. *Atomiz. Sprays* **23** (6), 541–565.

CASTREJÓN-PITA, J. R., CASTREJÓN-PITA, A. A., THETE, S. S., SAMBATH, K., HUTCHINGS, I. M., HINCH, J., LISTER, J. R. & BASARAN, O. A. 2015 Plethora of transitions during breakup of liquid filaments. *Proc. Natl Acad. Sci.* **112** (15), 4582–4587.

CHEN, Y. J. & STEEN, P. H. 1997 Dynamics of inviscid capillary breakup: collapse and pinchoff of a film bridge. *J. Fluid Mech.* **341**, 245–267.

CHRISTODOULOU, K. N. & SCRIVEN, L. E. 1992 Discretization of free surface flows and other moving boundary problems. *J. Comput. Phys.* **99** (1), 39–55.

CRASTER, R. V., MATAR, O. K. & PAPAGEORGIOU, D. T. 2002 Pinchoff and satellite formation in surfactant covered viscous threads. *Phys. Fluids* **14** (4), 1364–1376.

DAY, R. F., HINCH, E. J. & LISTER, J. R. 1998 Self-similar capillary pinchoff of an inviscid fluid. *Phys. Rev. Lett.* **80** (4), 704–707.

EGGERS, J. 1993 Universal pinching of 3D axisymmetric free-surface flow. *Phys. Rev. Lett.* **71** (21), 3458–3460.

EGGERS, J. 1997 Nonlinear dynamics and breakup of free-surface flows. *Rev. Mod. Phys.* **69** (3), 865–930.

EGGERS, J. 2005 Drop formation–an overview. *Z. Angew. Math. Mech.* **85** (6), 400–410.

EGGERS, J. & VILLERMAUX, E. 2008 Physics of liquid jets. *Rep. Prog. Phys.* **71** (3), 036601.

ELFRING, G. J., LEAL, L. G. & SQUIRES, T. M. 2016 Surface viscosity and Marangoni stresses at surfactant laden interfaces. *J. Fluid Mech.* **792**, 712–739.

FENG, J. Q. & BASARAN, O. A. 1994 Shear flow over a translationally symmetric cylindrical bubble pinned on a slot in a plane wall. *J. Fluid Mech.* **275**, 351–378.

FRANSES, E. I., BASARAN, O. A. & CHANG, C. H. 1996 Techniques to measure dynamic surface tension. *Curr. Opin. Colloid Interface Sci.* **1** (2), 296–303.

GOCKENBACH, M. S. 2006 *Understanding and Implementing the Finite Element Method*. SIAM.

GRESHO, P. M., LEE, R. L. & SANI, R. C. 1980 On the time-dependent solution of the incompressible Navier–Stokes equations in two and three dimensions. In *Recent Advances Numerical Methods in Fluids* (ed. C. Taylor & K. Morgan), pp. 27–79. Pineridge.

GRESHO, P. M. & SANI, R. L. 1998 *Incompressible Flow and the Finite Element Method. Volume 1: Advection-Diffusion and Isothermal Laminar Flow*. John Wiley and Sons.

HILZ, E. & VERMEER, A. W. P. 2013 Spray drift review: the extent to which a formulation can contribute to spray drift reduction. *Crop Protect.* **44**, 75–83.

KAMAT, P. M., WAGONER, B. W., THETE, S. S. & BASARAN, O. A. 2018 Role of Marangoni stress during breakup of surfactant-covered liquid threads: reduced rates of thinning and microthread cascades. *Phys. Rev. Fluids* **3** (4), 043602.

KOOIJ, S., SIJS, R., DENN, M. M., VILLERMAUX, E. & BONN, D. 2018 What determines the drop size in sprays? *Phys. Rev.* X **8** (3), 031019.

KOVALCHUK, N. M., NOWAK, E. & SIMMONS, M. J. H. 2016 Effect of soluble surfactants on the kinetics of thinning of liquid bridges during drops formation and on size of satellite droplets. *Langmuir* **32** (20), 5069–5077.

LI, Y. & SPRITTLES, J. E. 2016 Capillary breakup of a liquid bridge: identifying regimes and transitions. *J. Fluid Mech.* **797**, 29–59.

LIAO, Y. C., FRANSES, E. I. & BASARAN, O. A. 2006 Deformation and breakup of a stretching liquid bridge covered with an insoluble surfactant monolayer. *Phys. Fluids* **18** (2), 022101.

LISTER, J. R. & STONE, H. A. 1998 Capillary breakup of a viscous thread surrounded by another viscous fluid. *Phys. Fluids* **10** (11), 2758–2764.

MARTÍNEZ-CALVO, A., RIVERO-RODRÍGUEZ, J., SCHEID, B. & SEVILLA, A. 2020 Natural break-up and satellite formation regimes of surfactant-laden liquid threads. *J. Fluid Mech.* **883**, A35.

MARTÍNEZ-CALVO, A. & SEVILLA, A. 2018 Temporal stability of free liquid threads with surface viscoelasticity. *J. Fluid Mech.* **846**, 877–901.

MCGOUGH, P. T. & BASARAN, O. A. 2006 Repeated formation of fluid threads in breakup of a surfactant-covered jet. *Phys. Rev. Lett.* **96** (5), 054502.

MICHAEL, D. H. 1981 Meniscus stability. *Annu. Rev. Fluid Mech.* **13** (1), 189–216.

NEGIN, C., ALI, S. & XIE, Q. 2017 Most common surfactants employed in chemical enhanced oil recovery. *Petroleum* **3** (2), 197–211.

NOTTER, R. H. 2000 *Lung Surfactants: Basic Science and Clinical Applications*. CRC Press.

NOTZ, P. K. & BASARAN, O. A. 2004 Dynamics and breakup of a contracting liquid filament. *J. Fluid Mech.* **512**, 223–256.

PAPAGEORGIOU, D. T. 1995 On the breakup of viscous liquid threads. *Phys. Fluids* **7** (7), 1529–1544.

PATZEK, T. W., BENNER, R. E. JR., Basaran, O. A. & Scriven, L. E. 1991 Nonlinear oscillations of inviscid free drops. *J. Comput. Phys.* **97** (2), 489–515.

PLATEAU, J. 1873 *Experimental and Theoretical Statics of Liquids Subject to Molecular Forces Only*. Gauthier-Villars.

PONCE-TORRES, A., MONTANERO, J. M., HERRADA, M. A., VEGA, E. J. & VEGA, J. M. 2017 Influence of the surface viscosity on the breakup of a surfactant-laden drop. *Phys. Rev. Lett.* **118** (2), 024501.

RAYLEIGH, L. 1878 On the instability of jets. *Proc. Lond. Math. Soc.* **1** (1), 4–13.

ROCHÉ, M., AYTOUNA, M., BONN, D. & KELLAY, H. 2009 Effect of surface tension variations on the pinch-off behavior of small fluid drops in the presence of surfactants. *Phys. Rev. Lett.* **103** (26), 264501.

DE SAINT VINCENT, M. R., PETIT, J., AYTOUNA, M., DELVILLE, J. P., BONN, D. & KELLAY, H. 2012 Dynamic interfacial tension effects in the rupture of liquid necks. *J. Fluid Mech.* **692**, 499–510.

SCHEID, B., DELACOTTE, J., DOLLET, B., RIO, E., RESTAGNO, F., VAN NIEROP, E. A., CANTAT, I., LANGEVIN, D. & STONE, H. A. 2010 The role of surface rheology in liquid film formation. *Europhys. Lett.* **90** (2), 24002.

SCHEID, B., DORBOLO, S., ARRIAGA, L. R. & RIO, E. 2012 Antibubble dynamics: the drainage of an air film with viscous interfaces. *Phys. Rev. Lett.* **109** (26), 264502.

SCHUNK, P. R. & SCRIVEN, L. E. 1997 Surfactant effects in coating processes. In *Liquid Film Coating* (ed. S. F. Kistler & P. M. Schweizer), pp. 495–536. Springer.

SCRIVEN, L. E. 1960 Dynamics of a fluid interface equation of motion for newtonian surface fluids. *Chem. Engng Sci.* **12** (2), 98–108.

SHEN, A. Q., GLEASON, B., MCKINLEY, G. H. & STONE, H. A. 2002 Fiber coating with surfactant solutions. *Phys. Fluids* **14** (11), 4055–4068.

STEVENSON, P. 2005 Remarks on the shear viscosity of surfaces stabilised with soluble surfactants. *J. Colloid Interface Sci.* **290** (2), 603–606.

SUBRAMANI, H. J., YEOH, H. K., SURYO, R., XU, Q., AMBRAVANESWARAN, B. & BASARAN, O. A. 2006 Simplicity and complexity in a dripping faucet. *Phys. Fluids* **18** (3), 032106.

TIMMERMANS, M.-L. E. & LISTER, J. R. 2002 The effect of surfactant on the stability of a liquid thread. *J. Fluid Mech.* **459**, 289–306.

TRICOT, Y. M. 1997 Surfactants: Static and dynamic surface tension. In *Liquid Film Coating: Scientific Principles and Their Technological Implications* (ed. S. F. Kistler & P. M. Schweizer), pp. 99–136. Springer.

WEE, H., WAGONER, B. W., KAMAT, P. M. & BASARAN, O. A. 2020 Effects of surface viscosity on breakup of viscous threads. *Phys. Rev. Lett.* **124** (20), 204501.

WILKES, E. D. & BASARAN, O. A. 2001 Drop ejection from an oscillating rod. *J. Colloid Interface Sci.* **242** (1), 180–201.

XU, Q., LIAO, Y.-C. & BASARAN, O. A. 2007 Can surfactant be present at pinch-off of a liquid filament? *Phys. Rev. Lett.* **98** (5), 054503.

ZASADZINSKI, J. A., DING, J., WARRINER, H. E., BRINGEZU, F. & WARING, A. J. 2001 The physics and physiology of lung surfactants. *Curr. Opin. Colloid Interface Sci.* **6** (5–6), 506–513.

ZELL, Z. A., NOWBAHAR, A., MANSARD, V., LEAL, L. G., DESHMUKH, S. S., MECCA, J. M., TUCKER, C. J. & SQUIRES, T. M. 2014 Surface shear inviscidity of soluble surfactants. *Proc. Natl Acad. Sci.* **111** (10), 3677–3682.

ZHANG, X. & BASARAN, O. A. 1997 Dynamic surface tension effects in impact of a drop with a solid surface. *J. Colloid Interface Sci.* **187** (1), 166–178.

ZHANG, X., PADGETT, R. S. & BASARAN, O. A. 1996 Nonlinear deformation and breakup of stretching liquid bridges. *J. Fluid Mech.* **329**, 207–245.